17

Reprinted from JOURNAL OF THE ATMOSPHERIC SCIENCES, Vol. 46, No. 4, 15 February 1989
American Meteorological Society

Application of Vertical Normal Mode Expansion to Problems of Baroclinic Instability

AKIRA KASAHARA

National Center for Atmospheric Research, Boulder, Colorado*

H. L. TANAKA

Department of Atmospheric Science, University of Missouri-Columbia, Columbia, Missouri

(Manuscript received 25 February 1988, in final form 23 August 1988)

ABSTRACT

As an alternative to the finite difference method, we explore the use of the spectral method with normal modes as the basis functions for discretizing dependent variables in the vertical direction in order to obtain numerical solutions to time dependent atmospheric equations. The normal modes are free solutions to the time dependent perturbation equations linearized around the atmosphere at rest. To demonstrate the feasibility of normal mode representation in the spectral vertical discretization, the vertical normal mode expansion is applied to the quasi-geostrophic potential vorticity equation to investigate the traditional baroclinic instability of Charney and Green types on a zonal flow with a constant vertical shear. The convergence of the numerical solutions is examined in detail in relation to the spectral resolution of expansion functions.

We then extend the method of vertical normal mode expansion to solve the problem of baroclinic instability on the sphere. Two aspects are different from the earlier example. One is use of the primitive equations instead of the quasi-geostrophic system and the other is application of normal mode expansions in the horizontal, as well as vertical direction. First, we derive the evolution equations for the spectral coefficients of truncated series in three-dimensional normal mode functions by application of the Galerkin procedure to the global primitive equations linearized around a basic zonal flow with vertical and meridional shear. Then, an eigenvalue–eigenfunction problem is solved to investigate the stability of perturbation motions superimposed on the 30° jet examined earlier by Simmons, Hoskins and Frederiksen. From these two examples, it is concluded that the normal mode spectral method is a viable numerical technique for discretizing model variables in the vertical.

1. Introduction

There are two major approaches—finite difference and spectral—to numerically solve atmospheric prediction equations. Historically, the finite difference approach has been most prevalent in discretizing model variables. In recent years, however, the spectral method has been gaining popularity in discretizing model variables in the horizontal direction. In fact, most operational global forecast models now adopt spherical harmonic expansions to represent the model variables in the horizontal. For horizontal discretization of model variables, we now have the freedom of choice in selecting either the finite difference method or the spectral method.

For discretization of model variables in the vertical, our choice is very much limited to the finite difference method. Although some attempts have been made in the past, very few successful demonstrations are reported in the literature which suggest that the spectral method is a viable alternative to the finite difference method in discretizing model variables in the vertical.

There is one exception to this observation. A variant of the spectral method, called the finite element method (FEM), has been successfully applied. Staniforth (1985) reviews some of the recent developments in the application of the FEM to vertical discretization as well as to horizontal discretization of prediction models (see also Steppeler 1987). In the FEM, grid-point values are represented by basis functions which are piecewise polynomials spanning only local grid points centered around the grid point in question. Even though the Galerkin method (Finlayson 1972) is used to derive discretized prediction equations, their appearance is very much like that of finite difference equations. Moreover, the FEM lacks one of the unique features of the spectral method, namely the means to represent the variables in different scales.

The attempts to discretize model variables in the vertical using more traditional spectral techniques are rather limited. Francis (1972) proposed application of Laguerre polynomials in $\ln(p/p_s)$, where p is the pressure and p_s the surface pressure. He presented one ex-

* The National Center for Atmospheric Research is sponsored by the National Science Foundation.

Corresponding author address: Dr. Akira Kasahara, NCAR, P.O. Box 3000, Boulder, CO 80307-3000.

ample in which this application requires a very small time step to ensure a linear computational stability if the explicit time differencing scheme is used. The source of this difficulty was analyzed by Hoskins (1973). Machenhauer and Daley (1972) proposed use of Legendre polynomials for spectral representation in a p/p_s coordinate. However, we are not aware of any further attempt to follow through with their approach.

In the application of spectral techniques, the choice of basis functions is wide open. Bodin (1974) used the empirical orthogonal function (EOF) representation in the vertical to formulate a quasi-geostrophic prediction model. The EOFs are derived by minimizing the root-mean-square difference between the data and the functional representation (Obukhov 1960; Holmström 1963). The physics of the atmosphere is reflected statistically in the characteristics of the EOFs. Also, Grotjahn (1987) solved a baroclinic instability problem over a sphere using empirically defined orthogonal functions (which, however, are different from EOFs) to represent the vertical structure of the perturbation solutions. Another choice of basis functions is the eigensolutions of the vertical structure equation, referred to as normal modes, which are extensively used for the formulation of nonlinear normal mode initialization (Kasahara 1982). Gavrilin (1965) formulated a quasi-geostrophic prediction model, in which the vertical discretization uses orthogonal normal mode functions derived from the vertical structure equation for an atmosphere at rest. Simons (1968) describes the formulation of a quasi-geostrophic model along a similar approach, but the horizontal discretization uses spherical harmonic expansions so that the model is spectral in three-dimensions. To our knowledge, however, his model has never been fully tested.

Kasahara and Puri (1981) represented atmospheric data spectrally in three parameters (zonal wavenumber, meridional and vertical modal indices) using three-dimensional normal mode functions (3-D NMFs). The 3-D NMFs are constructed from the eigensolutions of a global primitive equation model and they are orthogonal functions. Kasahara (1984) formulated a linearized global spectral model with 3-D NMFs as the basis functions to investigate the time dependent response of model normal modes to tropical thermal forcing in the atmosphere at rest. This 3-D model formulation was extended by Kasahara and Silva Dias (1986, hereafter referred to as KS86), by considering the effects of a mean zonal flow with meridional and vertical shear. In this model configuration, it is possible to encounter the situation in which barotropic and/or baroclinic instability occurs. In order to avoid the occurrence of this situation, KS86 investigated only the steady response of planetary waves to stationary tropical heating.

Before treating the problem of barotropic/baroclinic instability over a sphere with the 3-D NMF expansion, we shall discuss the feasibility of solving the traditional Charney (1947)–Green (1960) baroclinic instability problem with vertical normal mode expansion. It is well known that the vertical structure equation which appears in the quasi-geostrophic model is identical to that in the primitive equation formulation. Therefore, we discuss in section 2 the applicability of vertical normal mode expansion to the quasi-geostrophic model. We are not aware of any earlier publication dealing with the problem of baroclinic instability by using vertical normal mode expansion, though spectral techniques have been used by other authors. For example, Simons (1969) adopted harmonic functions in the vertical and Boyd (1987) used rational Chebyshev functions defined on a semi-infinite interval for solving baroclinic instability problems. In section 3, we extend the use of vertical normal mode expansion to the problem of baroclinic instability over a sphere based on a linearized system of primitive equations. We use normal mode expansions in the horizontal as well, in order to solve the time dependent problem posed by KS86. In section 4, we present further discussions concerning the application of vertical normal mode expansion to atmospheric modeling. Conclusions are stated in section 5.

2. Quasi-geostrophic baroclinic instability

a. Basic equations

We choose a vertical coordinate σ ($\equiv p/p_s$, where p denotes the pressure and p_s the surface pressure, which is treated as a constant of 1000 hPa) and a horizontal coordinate $\tilde{x}$, directed eastward. Time is denoted by $\tilde{t}$. We consider perturbation motions superimposed on a mean basic zonal flow $\bar{u}(\sigma)$ which is a function of only σ.

The well-known equations of quasi-geostrophic flow on a beta-plane are combined into a potential vorticity equation for dependent variable $\tilde{\psi}$ (Kuo 1979). In dimensionless form, this equation is

$$\left(\frac{\partial}{\partial t}+U\frac{\partial}{\partial x}\right)\left\{\frac{\partial^2\psi}{\partial x^2}+\epsilon\frac{\partial}{\partial\sigma}\left[\frac{\sigma}{S}\frac{\partial\psi}{\partial\sigma}\right]\right\}+\left\{\beta-\epsilon\frac{\partial}{\partial\sigma}\left[\frac{\sigma}{S}\frac{\partial U}{\partial\sigma}\right]\right\}\frac{\partial\psi}{\partial x}=0 \quad (2.1)$$

which is to be solved subject to the upper and lower boundary conditions in dimensionless form

$$\left.\begin{aligned}\frac{\partial\psi}{\partial\sigma}&=0, \quad \text{at} \quad \sigma=\sigma_T\\ \left(\frac{\partial}{\partial t}+U\frac{\partial}{\partial x}\right)\frac{\partial\psi}{\partial\sigma}+r\frac{\partial\psi}{\partial t}&=\frac{dU}{d\sigma}\frac{\partial\psi}{\partial x}, \quad \text{at} \quad \sigma=1\end{aligned}\right\}. \quad (2.2)$$

In deriving the system of dimensionless equations (2.1) and (2.2), we use the notation shown in Table 1. The boundary conditions (2.2) are derived from the

TABLE 1. List of symbols.

L_*	Representative horizontal scale
H_*	Representative vertical scale in geometrical height
f_0	$(=2\Omega \sin\phi_0)$
β_0	$(=2\Omega \cos\phi_0/a)$
ϕ_0	Latitude of the beta-plane origin, which is chosen here at 45°N
g	Earth's gravity
Ω	Earth's angular speed
a	Earth's radius
t	$(=2\Omega\tilde{t})$ (scaled time)
x	$(=\tilde{x}/L_*)$ (scaled x-coordinate)
ψ	$(=\tilde{\psi}/H_*)$ (scaled dependent variable)
U	$[=\bar{u}/(2\Omega L_*)]$
β	$[=L_*\beta_0/(2\Omega)]$
ϵ	$[=(f_0L_*)^2/(gH_*)]$ (Lamb's parameter)
T_*	$(=gH_*/R)$
R	Specific gas constant of air
S	$[=(\kappa T_0/\sigma - dT_0/d\sigma)/T_*]$ (dimensionless static stability)
T_0	Basic state temperature as a function of σ
κ	$[=R/C_p\ (=2/7)]$
C_p	Specific heat at constant pressure
r	$(=ST_*/T_0)$ evaluated at $\sigma = 1$

statements that the perturbation temperature vanishes at the top, σ_T, and the vertical motion $d\psi/dt$ vanishes at the bottom, $\sigma = 1$.

b. *Vertical normal modes*

Solutions to (2.1) under boundary conditions (2.2) when the zonal mean flow is absent (i.e., $U = 0$) represent the normal modes of the system. In this case, (2.1) is separable in terms of two equations: one is referred to as the horizontal structure equation and the other as the *vertical structure equation* which is written in the form

$$\frac{d}{d\sigma}\left[\frac{\sigma}{S}\frac{dG}{d\sigma}\right] + \lambda G = 0, \tag{2.3}$$

where λ is the separation constant and $G(\sigma)$ denotes the vertical structure function. The boundary conditions (2.2) are now reduced to

$$\left.\begin{aligned} \frac{dG}{d\sigma} &= 0 \qquad \text{at} \quad \sigma = \sigma_T \\ \frac{dG}{d\sigma} + rG &= 0 \quad \text{at} \quad \sigma = 1 \end{aligned}\right\}. \tag{2.4}$$

The differential equation (2.3) together with the boundary conditions (2.4) forms a Sturm-Liouville problem which possesses a nontrivial solution only if the parameter λ is assigned one of a set of permissible values (Hildebrand 1958). For such a value of λ, say $\lambda = \lambda_n$, the system is satisfied by a solution of the form $G = CG_n(\sigma)$ where C is a constant. The permissible values of λ are known as its eigenvalues and the corresponding functions $G_n(\sigma)$ as the eigenfunctions or structure functions. Also, we find that any two eigenfunctions, G_i and G_j, are orthogonal. In terms of a new independent variable

$$Z = -\ln\sigma, \tag{2.5}$$

the orthogonality condition, in conjunction with a proper normalization, is expressed by

$$\int_0^{Z_T} G_iG_je^{-Z}dZ = \delta_{ij}, \tag{2.6}$$

where $Z_T = -\ln\sigma_T$.

For the basic state temperature profile $T_0(\sigma)$, we choose

$$T_0(\sigma) = (T_s - T_\infty)\exp(\kappa \ln\sigma) + T_\infty, \tag{2.7}$$

where $T_s = T_0(1)$. This temperature distribution is used by Pekeris (1937) and Gavrilin (1965). Figure 1 shows the temperature profile T_0 as a function of $Z\ (\equiv -\ln\sigma)$ for $T_s = 302.53$ K and $T_\infty = 83.265$ K after Fulton and Schubert (1980). We see that T_0 is representative of the mean tropospheric temperature distribution. For this temperature profile, the dimensionless static stability S in (2.3) is given by

$$S = \eta/\sigma, \tag{2.8}$$

where

$$\eta = \kappa T_\infty/T_*. \tag{2.9}$$

The solutions of the system (2.3) with (2.4) for the static stability (2.8) are discussed by Gavrilin (1965)

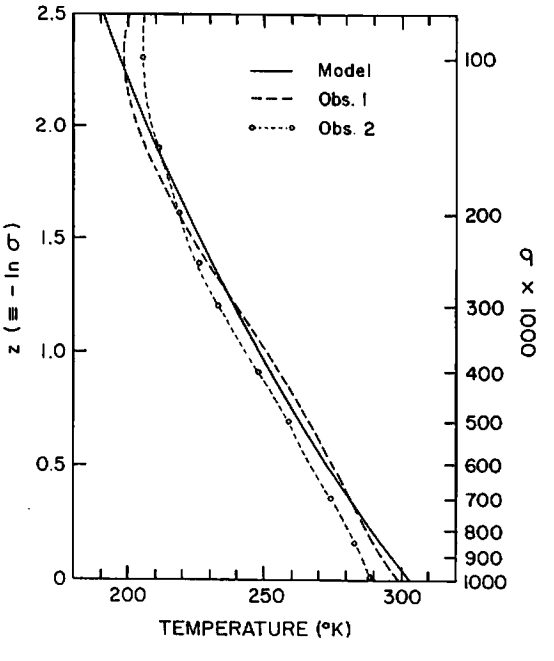

FIG. 1. Profile of T_0 as a function of $Z\ (\equiv -\ln\sigma)$. The scale for σ multiplied by 1000 is shown on the right. Obs. 1 denotes a mean tropical temperature distribution (Jordan 1958) and Obs. 2 a global mean temperature distribution during the FGGE (Tanaka 1985).

and Fulton and Schubert (1980). The eigenvalue λ_n in (2.3) can be expressed as

$$\lambda_n = H_*/D_n, \tag{2.10}$$

where D_n is referred to as the *equivalent height* (Taylor 1936).

1) EXTERNAL MODE

The mode corresponding to the largest value of D_n is called the *external mode*, indicated by the index $n = 1$. The value of D_1 is obtained by solving the transcendental equation

$$\left(\frac{RT_s}{gD_1} - \frac{1}{2}\right)\tanh(\mu Z_T) = \mu, \tag{2.11}$$

where

$$\mu^2 = \frac{1}{4} - \eta\frac{H_*}{D_1} > 0. \tag{2.12}$$

The eigenfunction G_1 is given by

$$G_1 = A_1\left[\sinh(\mu Z) - \frac{\mu}{(0.5 - r)}\cosh(\mu Z)\right]e^{Z/2}, \tag{2.13}$$

where

$$A_1 = \left\{\frac{1}{4\mu}\left[1 + \left(\frac{\mu}{0.5 - r}\right)^2\right]\sinh(2\mu Z_T) - 0.5Z_T\left[1 - \left(\frac{\mu}{0.5 - r}\right)^2\right] + \frac{1}{1 - 2r}[1 - \cosh(2\mu Z_T)]\right\}^{-1/2}. \tag{2.14}$$

2) INTERNAL MODES

The modes corresponding to the rest of the eigenvalues are called *internal modes*, indicated by index $n \geq 2$. The values of D_n are obtained by solving

$$\left(\frac{RT_s}{gD_n} - \frac{1}{2}\right)\tan(\xi_n Z_T) = \xi_n, \tag{2.15}$$

where

$$\xi_n^2 = \eta\frac{H_*}{D_n} - \frac{1}{4} > 0. \tag{2.16}$$

The eigenfunctions G_n are given by

$$G_n = A_n\left[\sin(\xi_n Z) - \frac{\xi_n}{(0.5 - r)}\cos(\xi_n Z)\right]e^{Z/2}, \tag{2.17}$$

where

$$A_n = \left\{\frac{-1}{4\xi_n}\left[1 - \left(\frac{\xi_n}{0.5 - r}\right)^2\right]\sin(2\xi_n Z_T) + 0.5Z_T\left[1 + \left(\frac{\xi_n}{0.5 - r}\right)^2\right] - \frac{1}{1 - 2r}[1 - \cos(2\xi_n Z_T)]\right\}^{-1/2}. \tag{2.18}$$

3) SPECIAL CASE

In solving the system (2.3) with (2.4) for the static stability (2.8), we assumed that

$$\mu^2 = \frac{1}{4} - \eta\lambda \neq 0. \tag{2.19}$$

There exists a nontrivial solution for $\mu^2 = 0$, if the top Z_T takes the value Z_{TC} defined by

$$Z_{TC} = \frac{4r}{1 - 2r}. \tag{2.20}$$

For the temperature distribution (2.7), the value of r becomes

$$r = \kappa T_\infty/T_s \quad (\equiv 0.0786368\cdots) \tag{2.21}$$

which gives $Z_{TC} = 0.37325\cdots$ (equivalently $\sigma_T = 0.6885$). Fulton and Schubert (1980) show that if $Z_T > Z_{TC}$ there exists a countable number of internal modes in addition to one external mode. We choose that $Z_T > Z_{TC}$.

4) PROFILES OF THE VERTICAL STRUCTURE FUNCTIONS

Figure 2 shows only the first twelve vertical profiles of eigenfunctions G_n as functions of $Z\,(= -\ln\sigma)$, calculated for the temperature distribution (2.7) and $Z_T = 2.5$. The values of equivalent height D_n in m are listed at the top.

c. *Normal mode expansions*

We transform the basic equation (2.1) using the independent variable $Z\,(\equiv -\ln\sigma)$. We then assume that

$$\psi = \Psi(Z)\exp[iK(x - Ct)], \tag{2.22}$$

where K is the dimensionless wavenumber scaled by the inverse of length scale L_*^{-1} and C is the dimensionless phase velocity scaled by $2\Omega L_*$. Also, Ψ denotes the amplitude function which depends on Z only.

Thus the basic equation (2.1) may be written as

$$(U - C)\left[K^2\Psi - \frac{\epsilon}{\eta}\left(\frac{d^2\Psi}{dZ^2} - \frac{d\Psi}{dZ}\right)\right] - \left[\beta - \frac{\epsilon}{\eta}\left(\frac{d^2U}{dZ^2} - \frac{dU}{dZ}\right)\right]\Psi = 0 \tag{2.23}$$

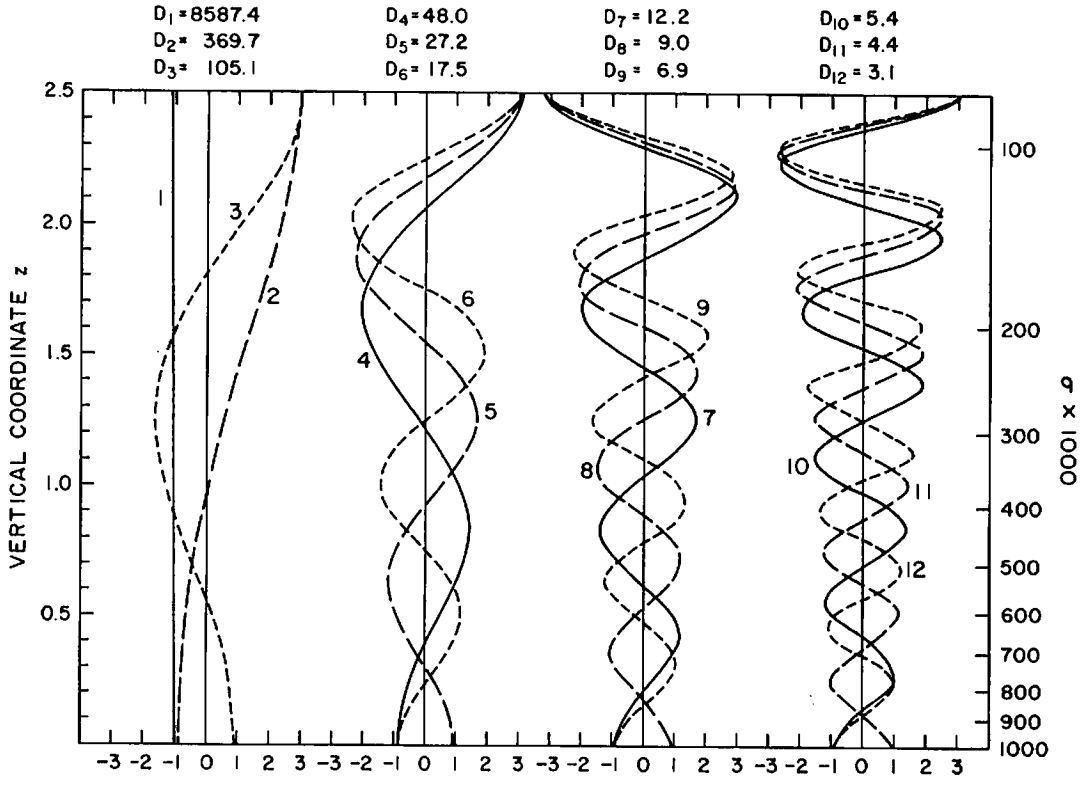

FIG. 2. Profiles of eigenfunctions G_n for the first twelve vertical modes as functions of Z. Numerals beside the profiles indicate modal index n. The values of equivalent height D_n are listed at the top.

and the corresponding boundary conditions (2.2) become

$$\frac{d\Psi}{dZ} = 0 \quad \text{at} \quad Z = Z_T, \tag{2.24a}$$

$$(U - C)\frac{d\Psi}{dZ} + rC\Psi = \frac{dU}{dZ}\Psi \quad \text{at} \quad Z = 0. \tag{2.24b}$$

We now assume that Ψ and U can be approximated by the following expansions

$$\Psi(Z) = \sum_{n=1}^{N} \frac{1}{\lambda_n} h_n G_n(Z), \tag{2.25}$$

$$U(Z) = \sum_{n=1}^{N} \alpha_n G_n(Z), \tag{2.26}$$

where N is a natural number and $G_n(Z)$, $N \geq n \geq 1$, are the eigenfunctions of (2.3) which satisfy the orthogonality condition (2.6). The coefficient α_n in (2.26) can be determined for a given distribution of $U(Z)$ by

$$\alpha_n = \int_0^{Z_T} U(Z) G_n e^{-Z} dZ. \tag{2.27}$$

It is important to observe that the expansions (2.25) and (2.26) permit Ψ to satisfy the boundary conditions (2.24), since each $G_n(Z)$ satisfies the boundary conditions (2.4).

Substituting (2.25) and (2.26) into (2.23), applying the vertical structure equation (2.3), multiplying the resulting equation by $G_l e^{-Z}$, integrating the result with respect to Z from 0 to Z_T, and utilizing the orthogonality condition (2.6), we obtain

$$C\left(1 + \frac{K^2}{\epsilon\lambda_n}\right)h_n + \frac{\beta}{\epsilon\lambda_n} h_n - \sum_{k=1}^{N}\left[\sum_{l=1}^{N} \alpha_l L_{lkn}\left(1 + \frac{K^2}{\epsilon\lambda_k} - \frac{\lambda_l}{\lambda_k}\right)\right]h_k = 0$$

$$\text{for} \quad n = 1, 2, \cdots, N, \tag{2.28}$$

where

$$L_{lkn} = \int_0^{Z_T} G_l G_k G_n e^{-Z} dZ. \tag{2.29}$$

Equation (2.28) is a system of $N \times N$ linear homogeneous equations. The phase velocity C is determined as an eigenvalue of this system for given values of parameters ϵ, β and K under a given form of $U(Z)$. The values of the interaction coefficient L_{lkn} are calculated from the vertical structure functions and the values of λ_n are calculated from the equivalent height. The vector h_n for $n = 1$ to N is the eigenfunction corresponding to the phase velocity C. Some of C may appear as complex conjugate pairs. In that case, unstable motions are expected from the imaginary

part C_i. The phase velocity is calculated from the real part C_r.

d. Results

We present results of the stability calculation for a linear basic zonal flow $U(Z) = \Lambda Z$, where $\Lambda = U_T/Z_T$ with U_T being the basic zonal velocity at $Z = Z_T$. It is important to note that the zonal flow $U(Z)$ in this problem is an approximation to the linear profile, since $U(Z)$ is expressed by a finite number of $G_n(Z)$ as shown by (2.26).

Figure 3a shows the growth rate $K|C_i|$ of the most unstable mode for resolution $N = 9$ as a function of the shear parameter U_T and the wavelength L ($\equiv 2\pi/K$). The same dimensionless symbols are used in the figure to indicate the units of corresponding dimensional quantities for simplicity. Figure 3b shows the phase velocity $C_r - U_M$, where $U_M = U_T/2$. We see the presence of a narrow stable region separating Charney (1947) and Green (1960) instability types. Note another instability maximum in the Charney type around $L = 2000$ km. For $L \leq 1000$ km, it is stable.

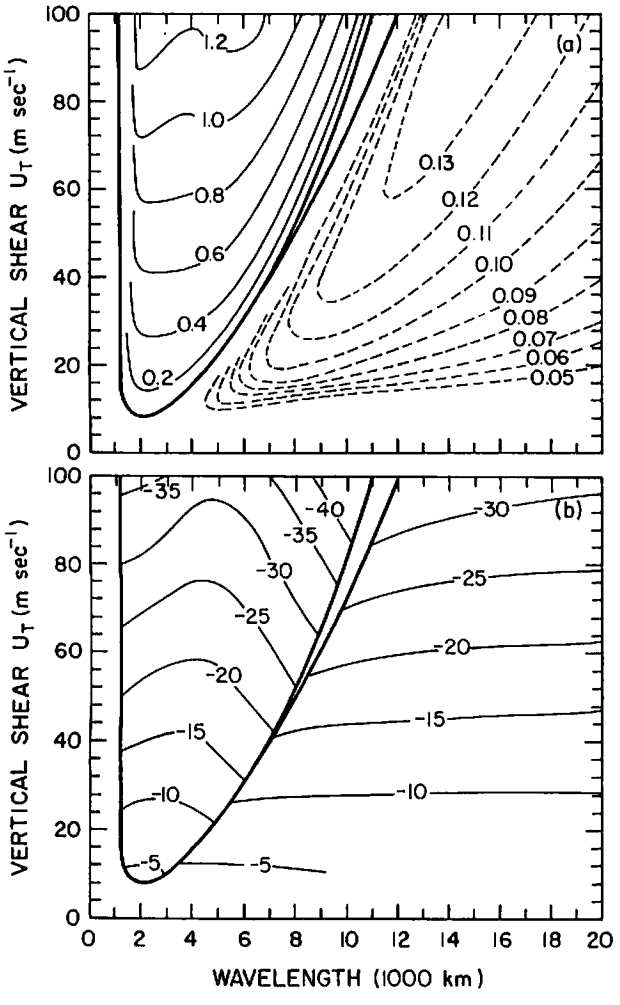

FIG. 3. (a) Growth rate $K|C_i|$ of the most unstable mode in units of day^{-1} for spectral resolution $N = 9$ as a function of vertical shear parameter U_T in m s^{-1} and wavelength L ($\equiv 2\pi/K$) in units of 1000 km. (b) As in (a), but for the phase speed $C_r - U_M$ in m s^{-1}, where $U_M = U_T/2$.

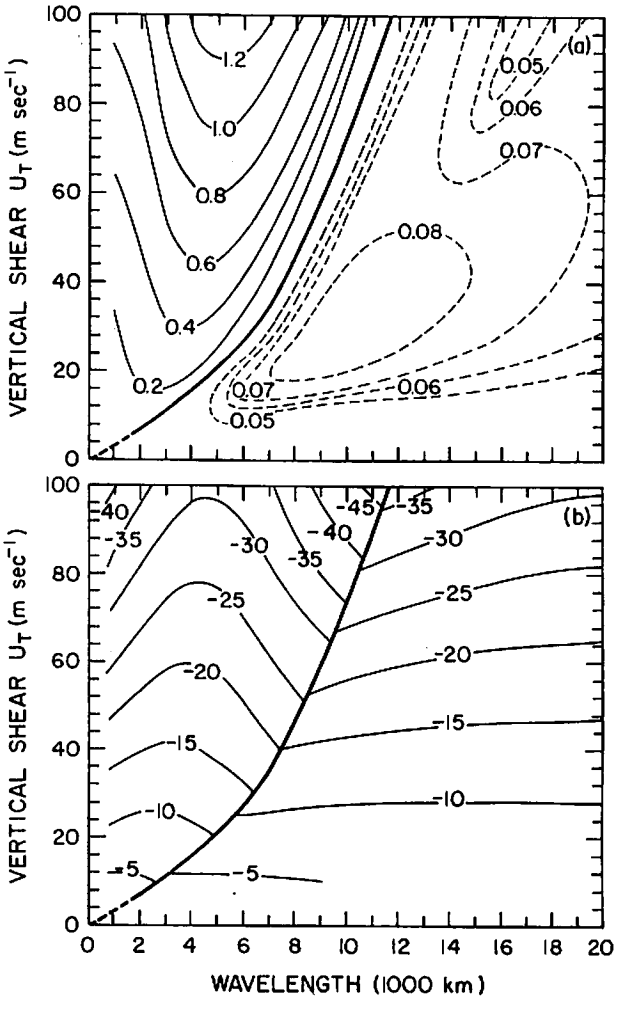

FIG. 4. As in Fig. 3a, b except the results are for resolution $N = 36$.

Figures 4a and 4b illustrate the same as Figs. 3a and 3b, except the results are for $N = 36$. Although the overall patterns are similar, we see differences in detail indicating the dependence of the solutions on resolution N. Actually, Fig. 4a resembles Fig. 6 of Garcia and Norscini (1970) and Kuo (1979) much closer than Fig. 3a. For example, now the region for $L \leq 1000$ km appears to be unstable, and the narrow stable region separating the Charney and Green types disappears. Also, the growth rate pattern of the Green modes seems to be credible. Next, we consider the question on the convergence of solution as modal resolution N increases.

Figure 5a shows the growth rate of the most unstable mode for wavelength L corresponding to 4000 km with the values of U_T corresponding to 100 m s^{-1} in solid line and U_T corresponding to 60 m s^{-1} in dashed line. Figure 5b illustrates the phase speeds for the same calculations. It is clear that the numerical solutions un-

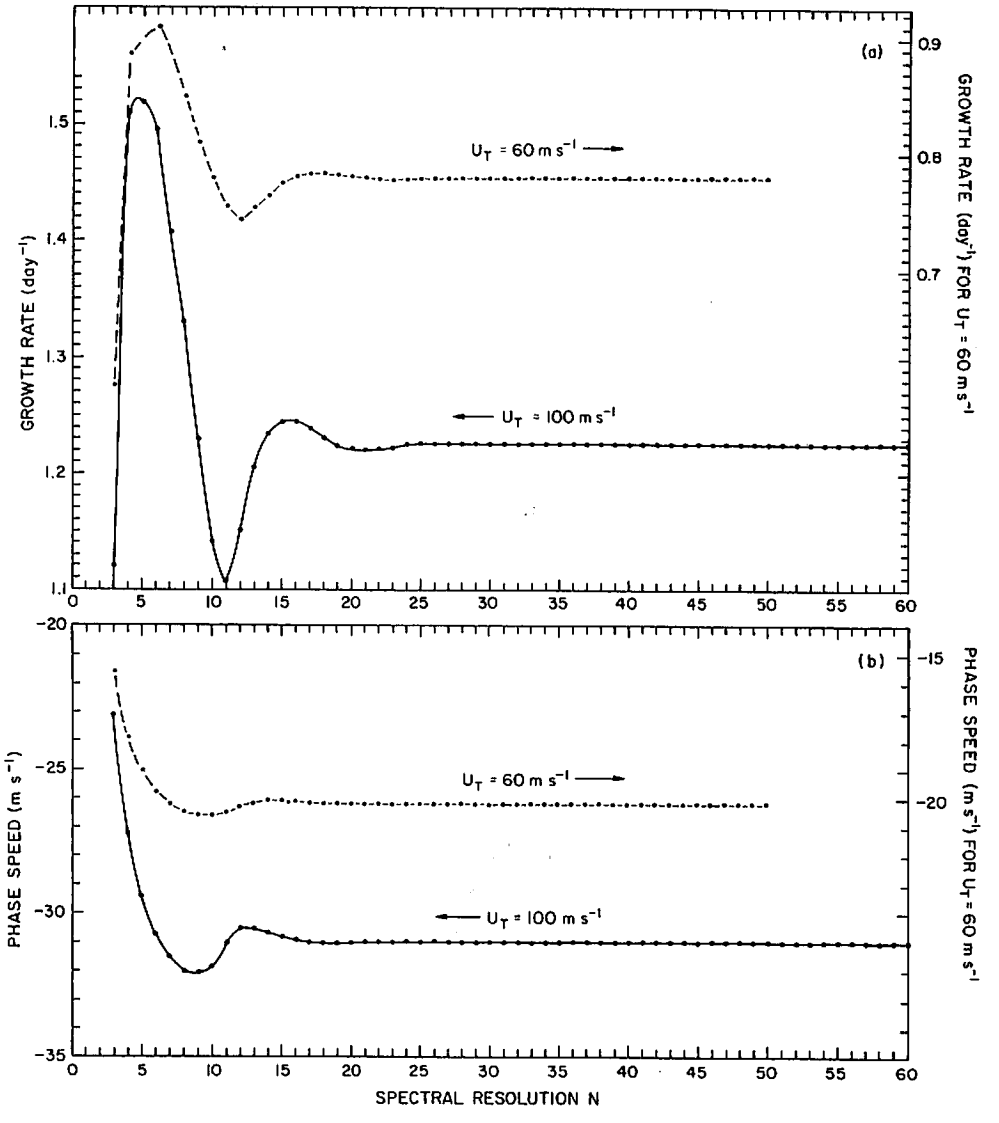

FIG. 5. (a) Growth rate of the most unstable mode as a function of vertical resolution N for L = 4000 km, U_T = 100 m s^{-1} (solid line) and U_T = 60 m s^{-1} (dashed line). (b) As in (a), but for the phase speed $C_r - U_M$ in m s^{-1}.

dergo a large variation with respect to N, but they quickly converge to common values once N becomes larger than about 25.

Figure 6 is the same as Fig. 5, except it concerns the case of L corresponding to 16 000 km. Notice a different manner of convergence of the solutions for Green modes. The convergence of solutions for U_T = 100 m s^{-1} is particularly slow, though we can say that the solutions practically converge beyond, say N = 50. The sensitivity of Green modes on modal resolution may explain the apparent differences in the growth rates of Green modes, particularly in the region of high vertical shear, between Figs. 3a and 4a.

In contrast, the vertical structures of the unstable motions do not appear to depend very strongly on spectral resolution. Figure 7 shows the vertical distributions of a normalized amplitude and the phase of ψ for L = 4000 km (upper panel) and L = 16 000 km (lower panel) with U_T = 100 m s^{-1}. We show the case of N = 9 by solid lines and that of N = 36 by dashed lines. Notice that the vertical structures of unstable motions for N = 9 and 36 are very close.

The growth rate and phase velocity of unstable motions and their vertical structure as calculated by the normal mode expansion are in agreement with those investigated by Green (1960), Hirota (1968), Garcia and Norscini (1970), Kuo (1979) and others by using different methods of solution. Although the growth rate and phase velocity of most unstable motions indicate the convergence of solutions as spectral resolution N increases, the manner of convergence exhibits irregular, damped oscillations. Staley (1986) reported the pres-

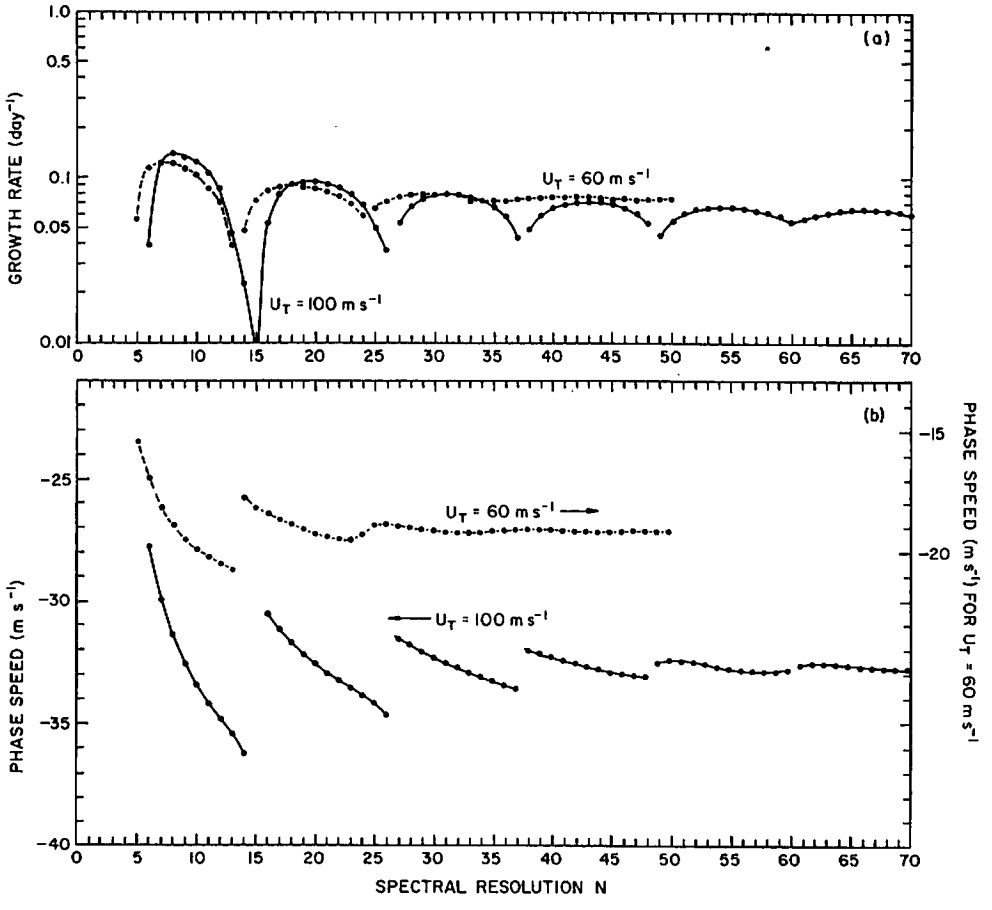

FIG. 6. As Fig. 5a, b, except the results are for L = 16 000 km.

ence of such a damped oscillation in convergence of solutions with the finite difference method. Also, Arakawa and Moorthi (1988) presented the results of baroclinic instability on a beta-plane which demonstrate that the growth rates converge in a damped oscillation manner as a function of the number of vertical levels used in their finite difference calculations in both short- and long-wave regimes. Therefore, it is not surprising that the numerical solutions converge in a damped oscillation manner as a function of the number of vertical modes used in the normal mode expansion. One possible explanation may lie in the findings of Lindzen and Tung (1978) and Lindzen et al. (1980) in which they suggest that baroclinic instability occurs as the result of the interaction of Rossby waves with critical levels involving wave propagation and trapping. The locations of critical levels in the basic zonal flow are different depending on the specific choice of spectral resolution N used in the vertical normal mode expansion of the basic zonal flow. In any event, as pointed out by Geisler and Garcia (1977), it is necessary to use a finer vertical resolution for accurately calculating the structure of baroclinically unstable motions when the vertical distribution of static stability has a large variation.

3. Baroclinic instability on the sphere

We now extend the method of vertical normal mode expansion to solve the problem of baroclinic instability on the sphere. Two aspects are different from the discussions presented in section 2. One is the use of the primitive equations instead of the quasi-geostrophic system and the other is application of the normal mode expansion method to the horizontal directions. The choice of spherical coordinates instead of Cartesian coordinates becomes only relevant in the selection of basis functions in the spectral expansion. Therefore, the basic formulation presented below is applicable to other coordinate systems, such as midlatitude and equatorial beta planes and even the f plane, by selecting suitable normal modes as the basis functions in the horizontal directions. In the following presentations, we use the same notation for variables and parameters as in section 2. One deviation is the use of the vertical coordinate defined by

$$\sigma = 2p/p_s - 1 \tag{3.1}$$

which is rescaled to give $\sigma = -1$ at the top ($p = 0$), while the lower boundary, $p = p_s$ which is treated as a constant of 1000 hPa, is located at $\sigma = 1$.

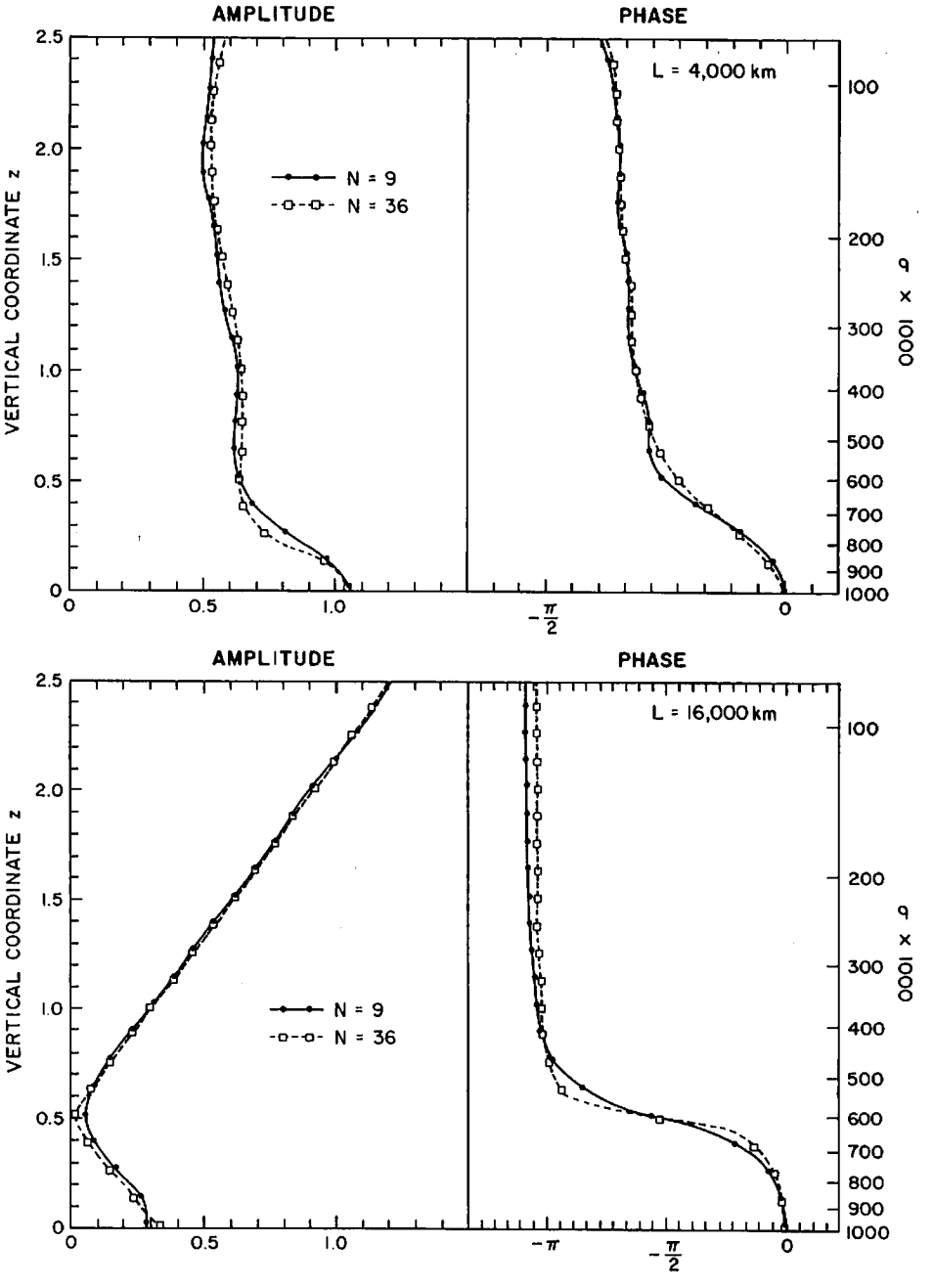

FIG. 7. Upper panel: Vertical distributions of a normalized amplitude and the phase of ψ for $L = 4000$ km and $U_T = 100$ m s^{-1}. Lower panel: As in the upper panel, but for $L = 16\,000$ km.

In the horizontal directions, we adopt spherical coordinates of longitude λ and latitude ϕ, increasing eastward and northward, respectively. The distinction between longitude λ and eigenvalue λ_n should be clear.

a. Basic equations

In deriving the linearized system for perturbation variables, we express

- Zonal velocity component = $\bar{u}(\phi, \sigma) + u'(\lambda, \phi, \sigma, \tilde{t})$;
- Meridional velocity component = $v'(\lambda, \phi, \sigma, \tilde{t})$;
- Vertical σ velocity $d\sigma/d\tilde{t} = \omega'(\lambda, \phi, \sigma, \tilde{t})$;
- Temperature = $T_0(\sigma) = \bar{T}(\phi, \sigma) + T'(\lambda, \phi, \sigma, \tilde{t})$;
- Isobaric height = $Z_0(\sigma) + \bar{Z}(\phi, \sigma) + Z'(\lambda, \phi, \sigma, \tilde{t})$;

where $T_0(\sigma)$ and $Z_0(\sigma)$ represent the global mean temperature distribution and the corresponding isobaric height distribution which are connected hydrostatically. Also, $\bar{u}(\phi, \sigma)$ is the basic zonal wind, while

$\bar{T}(\phi, \sigma)$ and $\bar{Z}(\phi, \sigma)$ constitute the deviations of the basic temperature and isobaric height from their global mean values $T_0(\sigma)$ and $Z_0(\sigma)$. These three fields are connected by the hydrostatic equation and a gradient wind relation. The perturbation quantities are denoted by primes.

We use the system of linearized equations, derived in KS86, based on the equations of horizontal motion, continuity and thermodynamics. These equations are given by (2.10) in KS86 in which the frictional, thermal dissipative and forcing terms are neglected in this study. We seek the solutions of the equations by using the method of normal mode expansion discussed in KS86. This idea originates from the expansion theorem of Eckart (1960, Chapter 6). Let the dependent variables be defined in the vector form

$$\mathbf{W}(\lambda, \phi, \sigma, t) = [u, v, z]^{\mathrm{T}} \tag{3.2}$$

where u, v and z are dimensionless dependent variables as defined by (2.9a) in KS86 without tildes. We express $\mathbf{W}$ in the form

$$\mathbf{W} = \sum_n \sum_s \sum_r \begin{pmatrix} \lambda_n^{-1/2} \\ \lambda_n^{-1/2} \\ \lambda_n^{-1} \end{pmatrix} \times W_r^s(n; t)\mathbf{H}_r^s(\phi; n)G_n(\sigma)e^{is\lambda}. \tag{3.3}$$

Here, the function $G_n(\sigma)$ denotes the vertical structure of the normal modes and λ_n is the associated eigenvalue (normalized equivalent height) of the vertical structure equation as described by Kasahara (1984, hereafter referred to as K84). The subscript n denotes the index of the vertical modes. The function $\mathbf{H}_r^s$ denotes the meridional structure of the normal modes, which depends on the vertical modal index n as well as the zonal wavenumber s. The subscript r refers to a serial index for the westward and eastward-propagating gravity waves and the westward propagating rotational (Rossby) waves as the first and second kinds of shallow-water waves (e.g., Longuet-Higgins 1968). The Hough vector function $\mathbf{H}_r^s$ is calculated using a software developed by Swarztrauber and Kasahara (1985). The coefficient $W_r^s(n; t)$ is a scalar which is a function of t. The series (3.3) consists of the summations with respect to three indices, n for vertical mode, s for zonal wavenumber, and r for all meridional modes of the westward and eastward-propagating inertia–gravity waves and rotational (Rossby) modes.

The evolution of the spectral coefficients $W_r^s(n; t)$ is determined by the system of ordinary differential equations in time which are obtained from (2.10) of KS86 by application of the Galerkin technique (Finlayson 1972). To this end, we substitute the expression (3.3) into (2.10) of KS86, multiply the result by the weight of $\mathbf{H}_{r'}^{s'*}(\phi; n')G_{n'}(\sigma)\exp(-is'\lambda)$, and integrate the resulting equations with respect to λ from 0 to 2π, σ from -1 to 1, ϕ from $-\frac{1}{2}\pi$ to $\frac{1}{2}\pi$. Note that the superscript asterisk denotes complex conjugation. The result can be greatly simplified because of the orthogonality conditions for the zonal harmonic functions, Hough vector functions, and vertical structure functions.

Thus, we obtain the following spectral equations to describe the temporal evolution of the spectral coefficients W_r^s for various combinations of n, s and r:

$$dW_r^s(n; t)/dt + i\nu_r^s(n)W_r^s(n; t) = N_r^s(n), \tag{3.4}$$

where

$$N_r^s(n) = \int_{-\pi/2}^{\pi/2} \mathbf{N}_s(n; \phi) \cdot \mathbf{H}_r^{s*}(\phi; n) \cos\phi d\phi, \tag{3.5}$$

$$\mathbf{N}_s(n; \phi) = (2\pi)^{-1} \int_0^{2\pi} \mathbf{N}_n(\lambda, \phi)e^{-is\lambda}d\lambda, \tag{3.6}$$

$$\mathbf{N}_n(\lambda, \phi) = \int_{-1}^{1} \mathbf{N}(\lambda, \phi, \sigma)G_n(\sigma)d\sigma, \tag{3.7}$$

$$\mathbf{N}(\lambda, \phi, \sigma) = [\lambda_n^{1/2}A, \lambda_n^{1/2}B, \partial C/\partial\sigma]^{\mathrm{T}}. \tag{3.8}$$

Here, A, B and C are defined by (2.11) in KS86 without the thermal forcing term. In (3.4), $\nu_r^s(n)$ denotes the frequency of the normal modes obtained from the eigenvalue-eigenfunction problem shown by (3.15) in KS86. The presence of the second term on the left-hand side of (3.4) reflects the fact that the strictly linear part of (2.10) in KS86 (by setting the right-hand sides to zero) give the normal mode solutions.

Integral (3.7) is the vertical transform of the nonhomogeneous terms. Integral (3.6) is the Fourier transform and integral (3.5) denotes the Hough transform. Kasahara (1977, 1978) describes how to calculate (3.6) and (3.5). The form of spectral equation (3.4) is discussed in general terms by Eckart (1960, Chapter 6) and a special case of the nondivergent vorticity equation is treated by Platzman (1960).

b. Stability problem

We use the 3-D normal mode expansion method to investigate the problem of baroclinic instability on a sphere. As a specific example, we examine the case of the 30° jet of Simmons and Hoskins (1976), described in the Appendix, for the basic flow. We seek the solution of (3.4) in the form

$$W_r^s(n; t) = C_r^s(n)e^{-i\nu t}, \tag{3.9}$$

where ν is the frequency and $C_r^s(n)$ denotes the complex amplitude of oscillation. We consider the perturbation variables that can be represented by only one zonal wavenumber component s, which is given by a natural number. When we solve for ν, some of the frequency may appear as complex conjugate pairs; unstable motions are expected from a positive imaginary part of ν.

For the basic temperature distribution $T_0(\sigma)$ given in the Appendix, the vertical structure function $G_n(\sigma)$ and the normalized equivalent height λ_n are solved by using the numerical method described in the Appendix of K84. Table 2 shows the values of equivalent height D_n ($\equiv H_*/\lambda_n$) in m and gravity wave speed $\sqrt{gD_n}$ in m s^{-1}. These values are very similar to those given in Table A2 of K84. The vertical distributions of G_n (not shown) are also very similar to those shown in Fig. A1 of K84.

For the meridional resolution, we selected (as in KS86) a total of 17 modes, consisting of 16 rotational modes plus the Kelvin mode, for each vertical mode. The number of rotational modes is decided considering the spectral distribution of atmospheric energy in terms of rotational modes as obtained by Tanaka (1985). Gravity modes do not play any significant role in the present instability calculations (see Tanaka 1988). The Kelvin mode is symmetric with respect to the equator. Among 16 rotational modes, one-half are symmetric and the rest are antisymmetric with respect to the equator.

After substituting (3.9) into (3.4), we carry out the calculation of the three integrals (3.5), (3.6) and (3.7), remembering that the terms A, B and C are defined in (2.11) of KS86. The factor $\exp(-ivt)$ can be removed from the resulting equations, leaving the following system of equations:

$$[\nu^s_{r'}(n) - \nu]C^s_{r'}(n) + \sum_{k=1}^{N}\sum_{r=1}^{R} \mathbf{b}^s_{r'r}(n, k)C_r^s(k) = 0 \tag{3.10}$$

for $r' = 1, 2, \cdots, R$; $n = 1, 2, \cdots, N$. Here, the natural numbers N and R are chosen to be 6 and 17, respectively, corresponding to our specific modal resolution. A single natural number, s, specifies the zonal wavenumber. In (3.10), $\mathbf{b}^s_{r'r}(n, k)$ is the following matrix:

$$\mathbf{b}^s_{r'r}(n, k) = \sum_{l=1}^{N} L_{lnk}\left(\frac{\lambda_n}{\lambda_k}\right)^{1/2}\beta_l \int_{-\pi/2}^{\pi/2}\Bigg[s\bar{\alpha}_0(\phi)\Bigg\{U_r^s(\phi; k)U^s_{r'}(\phi; n) + V_r^s(\phi; k)V^s_{r'}(\phi; n) + \left(\frac{\lambda_k}{\lambda_n}\right)^{1/2} Z_r^s(\phi; k)Z^s_{r'}(\phi; n)\Bigg\} + 2\bar{\alpha}_0(\phi)\sin\phi\{V_r^s(\phi; k)U^s_{r'}(\phi; n) + U_r^s(\phi; k)V^s_{r'}(\phi; n)\}$$
$$- \frac{d\bar{\alpha}_0(\phi)}{d\phi}\cos\phi V_r^s(\phi; k)U^s_{r'}(\phi; n) + \frac{1}{\gamma}\bar{\alpha}_0(\phi)\sin\phi\cos\phi V_r^s(\phi; k)Z^s_{r'}(\phi; n)\frac{\lambda_l}{\sqrt{\lambda_n}}\Bigg]\cos\phi d\phi, \tag{3.11}$$

where

$$L_{lnk} = \int_{-1}^{1} G_l G_n G_k d\sigma \tag{3.12}$$

denotes the triple-interaction coefficients for various combinations of vertical modal indices l, n and k. A similar integral has already appeared in section 2 as (2.29). The significance of this integral is discussed in KS86 regarding the role of the vertical shear of the zonal mean wind for providing energy transfer among different vertical modes. In (3.11), quantities $\bar{\alpha}_0(\phi)$ and β_l are related to the basic zonal flow and are defined by (A4) and (A5) in the Appendix.

TABLE 2. Values of equivalent height D_n in m and gravity wave speed $\sqrt{gD_n}$ in m s^{-1}.

Vertical mode n	D_n (m)	$\sqrt{gD_n}$ (m s^{-1})
1	9641.785	309.39
2	3029.302	172.30
3	702.583	82.98
4	186.226	42.72
5	62.537	24.76
6	23.677	15.23
7	9.274	9.534
8	2.697	5.141
9	0.248	1.559

The system of equations (3.10) constitutes an eigenfunction–eigenvalue problem $(\mathbf{M} - \nu\mathbf{I})\mathbf{X} = 0$ where

$$\mathbf{X} = [C_1^s(1), C_2^s(1), \cdots, C_R^s(1), C_1^s(2), C_2^s(2), \cdots, C_R^s(2), \cdots, C_1^s(N), C_2^s(N), \cdots, C_R^s(N)]^{\mathrm{T}} \tag{3.13}$$

denotes the eigenvector with 102 elements for $N = 6$ and $R = 17$. The corresponding eigenvalue is ν. Here, $\mathbf{M}$ is a 102×102 square matrix (not shown). Once the elements C_r^s of $\mathbf{X}$ and ν are determined, the solution (3.3) is obtained with the aid of (3.9).

c. *Growth rates and phase speeds*

Growth rates and phase speeds as functions of wavenumber s for the 30° jet of Simmons and Hoskins (1976, hereafter referred to as SH76) are presented in Fig. 8. The results from the two vertical resolutions $N = 5$ and $N = 6$ are included in the same figure. These are for the fastest growing unstable symmetric modes designated as S1, which is the lowest symmetric meridional mode. We show also the results of SH76 for the corresponding case obtained with the linear primitive equation (PE) and quasi-geostrophic (QG) spherical harmonic spectral models using the horizon-

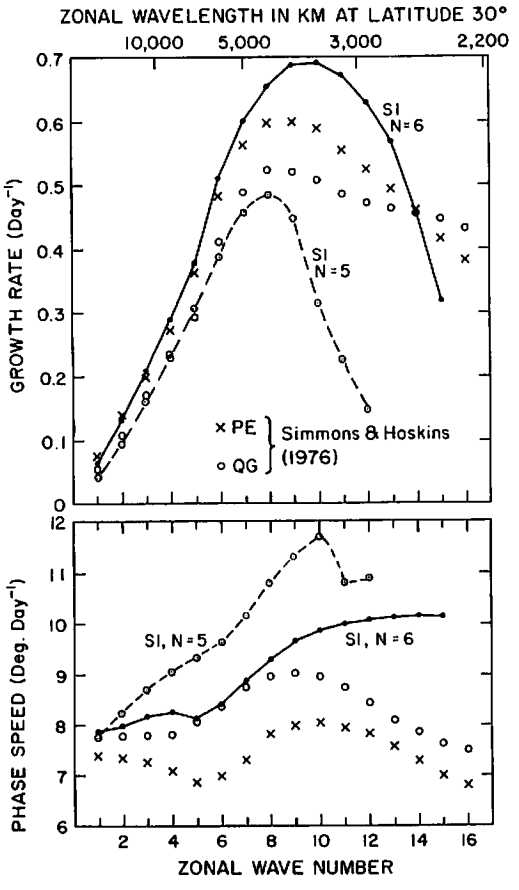

FIG. 8. Growth rates (a) and phase speeds (b) as functions of wavenumber s for the 30° jet for the most unstable symmetric mode designated as S1 for two vertical resolutions $N = 5$ and 6.

tal resolution of rhomboidal 31 and the vertical resolution of eight layers. The unstable modes were determined by using the initial-value approach. The growth rates of unstable modes up to wavenumber seven or eight are in general agreement with those of SH76. The phase speeds, however, are sensitive to the vertical resolution even in planetary scales. We notice discrepancies between our results with those of SH76 in both growth rates and phase speeds for wavenumbers greater than 7 or 8.

Before we comment on the cause of these discrepancies, let us present Fig. 9 which depicts results of the second most unstable symmetric modes (S2) for two vertical resolutions $N = 5$ and 6. The corresponding PE results obtained by SH76 and the corresponding QG results by Frederiksen (1978, hereafter referred to as F78) are also shown. Frederiksen adopted the eigenvalue approach to the same 30° jet using a quasi-geostrophic spherical harmonic spectral model with the horizontal resolution of rhomboidal 29 and the vertical resolution of eight levels. The growth rates of our calculations agree in general with those of SH76 and F78 for wavenumbers less than eight, but the discrepancies in phase speeds are noticeable. In general, results of F78 are in very good agreement with those of SH76. This is also the case of the first unstable S1 mode, though we did not plot the F78 results on Fig. 8.

On Figs. 8 and 9, we notice discrepancies between our results and those of SH76 and F78 in both growth rates and phase speeds for wavenumbers greater than 8. From the results of two calculations with vertical resolution $N = 5$ and 6, we find that short-wave behaviors are very sensitive to vertical resolution. As discussed by Simmons and Hoskins (1977), Gall and Blakeslee (1977), and Valdes and Hoskins (1988), the differences in short-wave behavior depend on many factors. Slight differences in basic states, model formulations (quasi-geostrophic vs. primitive equation) and horizontal resolution are all likely to be of importance in addition to vertical resolution in explaining the differences. Tanaka (1988) performed a vertical resolution experiment for baroclinic instability on a beta-plane with the vertical normal mode expansion and found that the solutions nearly converge with $N = 6$ for wavenumber 2, $N = 8$ for wavenumber 6, but wavenumber 10 appears to require $N > 20$ for convergence.

Because the meridional expansions of variables involve both symmetric and antisymmetric functions, though the basic flow is symmetric with respect to the equator, we obtain unstable solutions which are antisymmetric, as well as symmetric with respect to the

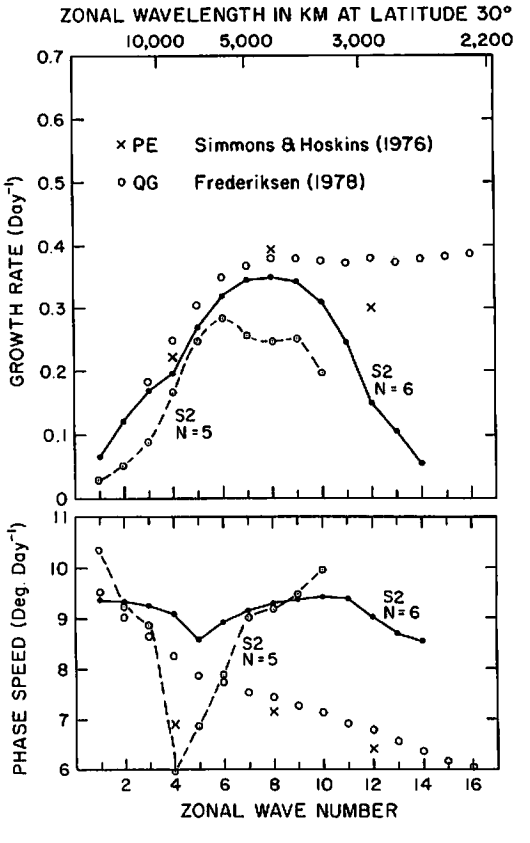

FIG. 9. As in Fig. 8, but for the second most unstable symmetric mode designated as S2.

equator. Figure 10 is like Figs. 8 and 9, except it considers the first and second unstable antisymmetric modes A1 and A2. The growth rates and phase speeds of A1 and A2 are very similar to those of S1 and S2. Simmons and Hoskins (1976) also noted the similarity of growth rates and phase speeds of S1 and A1 for wavenumbers 4 and 8. One aspect which appears to be different is that the growth rates of A2 for wavenumbers 1 and 2 are slightly larger than those of A1. Therefore, A1 modes are not necessarily the most unstable modes, while S1 modes are found to be the most unstable modes.

As seen from Frederiksen (1978), Hoskins and Revell (1981), and Ioannou and Lindzen (1986), it is possible to find still higher unstable modes with slower growth rates and increased meridional complexity in their structure. Figure 11 shows the growth rates and phase speeds of the third and fourth symmetric and antisymmetric modes, S3, A3, S4 and A4 in the case of $N = 6$. While the growth rates of S3 and S4 are comparable to those obtained by F78, our results show that the maximum values are present at intermediate wavenumbers, whereas those of F78 monotonically in-

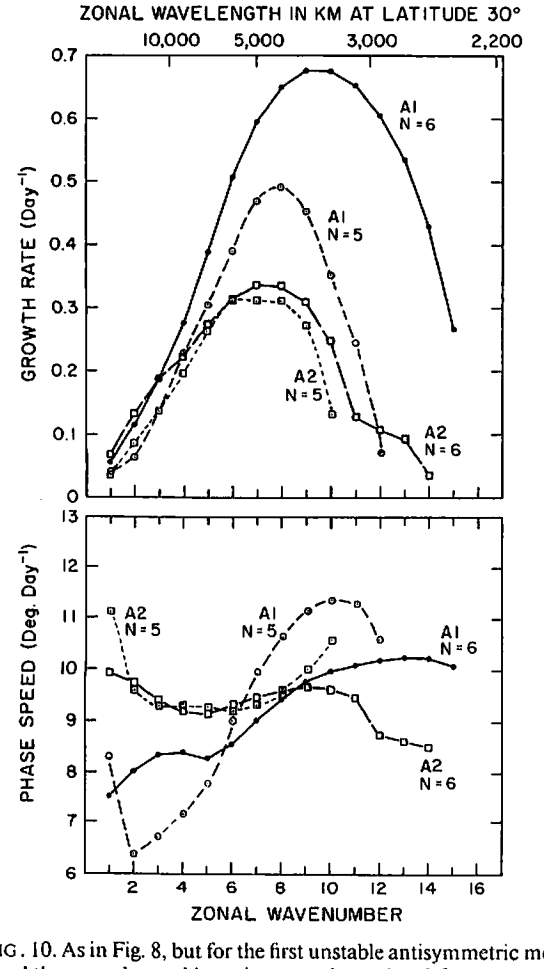

FIG. 10. As in Fig. 8, but for the first unstable antisymmetric mode A1 and the second unstable antisymmetric mode A2 for two vertical resolutions $N = 5$ and 6.

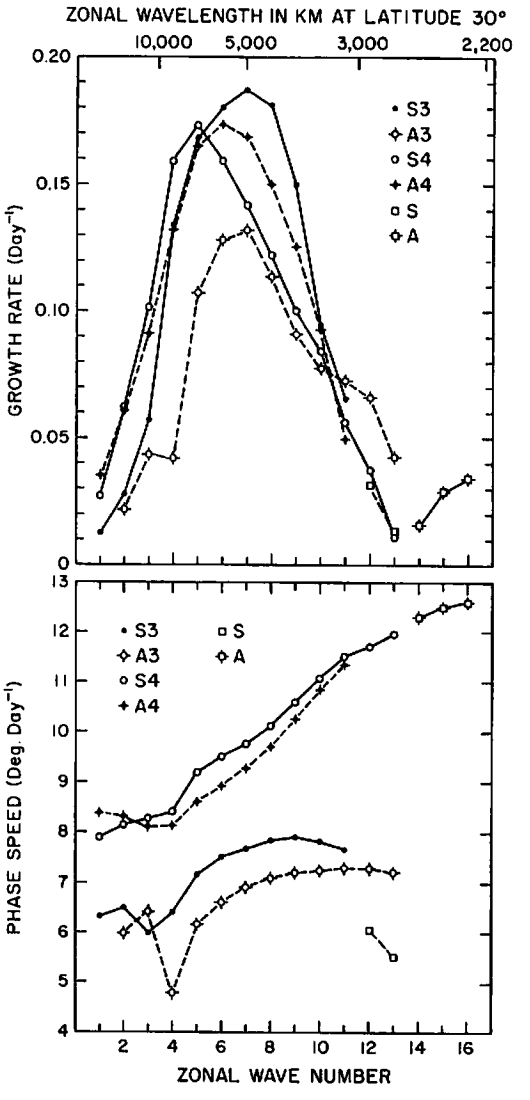

FIG. 11. Growth rates and phase speeds as functions of wavenumber s for the third most unstable symmetric S3 mode and antisymmetric A3 mode and the fourth most unstable symmetric S4 mode and antisymmetric A4 mode for vertical resolution $N = 6$.

crease with respect to zonal wavenumber. Since the higher unstable modes are associated with higher meridional complexity, their accuracies are very much subject to the meridional resolution of the basis functions. We should note, however, that the growth rate characteristics of our study are in general agreement with those of Ioannou and Lindzen (1986), who state that the maximum growth rate of unstable modes in a jet type shear flow occurs around zonal wavenumber 8 and that the maximum growth rates for higher modes tend to shift toward smaller zonal wavenumber.

The disappearance of the separation between the growth rates of the Charney and Green types, discussed in section 2, in the growth rates for the 30° jet is explained by Hoskins and Revell (1981). They showed that the small growth rates in the Charney and Green types for long waves are due to the lack of meridional

variation. When this restriction is removed and the meridional variation of motion is included, the growth rates of baroclinic instability between Cartesian and spherical coordinate systems show good agreement. The meridional scale of instability is determined by the breadth of zonal flow jets.

d. Structures of unstable modes

Figure 12 shows the distributions of amplitude (solid lines) and phase (dash lines) of the S1 and A1 modes in the case of $N = 6$ for zonal wavenumber $s = 4$ as functions of latitude ϕ and vertical coordinate p/p_s. The figure shows only the Northern Hemisphere. The distributions in the Southern Hemisphere follow the property of symmetry. The maximum intensities of the S1 mode (upper panel) and A1 mode (lower panel) are both found around $p/p_s = 0.4$ and 42°N. In both cases, the phase decreases upward and also northward and southward of 44°N. The northward decrease of phase in the lower troposphere is sharper than the southward decrease. In the upper troposphere, the northward and southward decrease from the latitude of, say, 43°N are more or less even.

The horizontal structures of the S1 and A1 modes at a lower level ($p/p_s = 0.870$) and an upper level ($p/p_s = 0.227$) are shown in Fig. 13. These levels are indicated by L.L. and U.L. on the left side of Fig. 12. Between L.L. and U.L. there are phase differences of almost 180° for both the S1 and A1 modes. This is clearly seen from Fig. 13 as almost out of phase patterns between the right and left side panels. With the help of the horizontal patterns of Fig. 13, the previous discussion on the amplitude and phase diagrams of Fig. 12 becomes apparent in visualizing the three-dimensional structures of the S1 and A1 modes. The velocity fields are shown on Fig. 13 by arrows with the scale indicated on the lower right-hand corner. Actually, the magnitudes of unstable motions are so chosen that the contour interval is 5 m and the maximum velocity is 5 m s^{-1}. It is clear that the three-dimensional structures of the S1 and A1 modes are very similar.

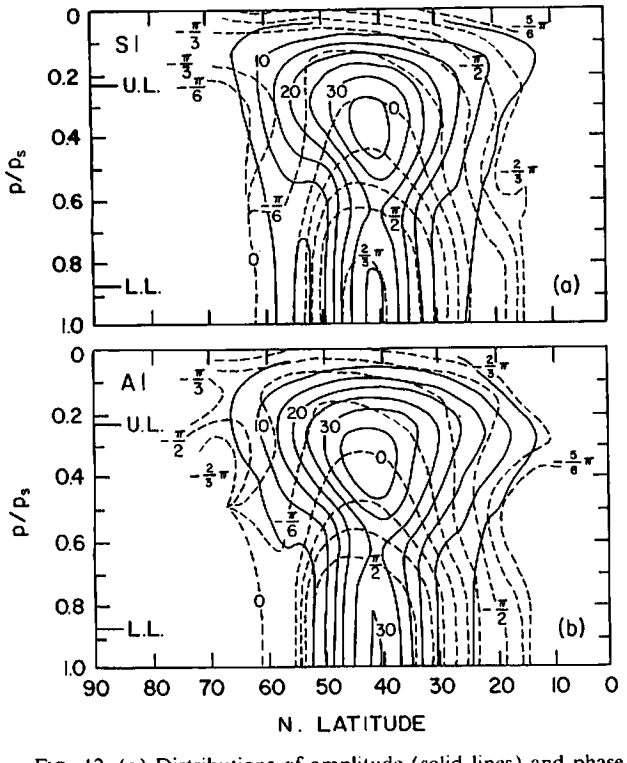

FIG. 12. (a) Distributions of amplitude (solid lines) and phase (dash lines) of S1 mode for zonal wavenumber 4 as functions of north latitude ϕ and vertical coordinate p/p_s. (b) As in (a), but for the A1 mode.

Figures 14 and 15 are the same as Figs. 12 and 13 respectively, except they depict the S2 and A2 modes. In general, the three-dimensional structures of the S2 and A2 modes are very similar, so we will concentrate on discussing the structure of S2 mode below. The maximum amplitude is found around the level $p/p_s = 0.35$ at 50°N, while in the lower troposphere there are two maxima, the major one around 46°N and the minor one around 33°N. In fact, the upper left panel in Fig. 15 is very much representative of the S2 structure in the lower troposphere. The phase decreases upward and northward of 30°N. (The phase also decreases southward from 30°N, but the amplitude becomes very small towards the equator.) One different aspect of the S2 structure compared with the S1 structure is that the system is stretched in the northwest–southeast direction throughout the troposphere, while the S1 structure in the lower troposphere stretches more or less in the opposite direction, i.e., the northeast–southwest direction. This suggests that the S1 and S2 modes have very different roles in the horizontal eddy momentum transport mechanism. As far as the vertical tilt of the trough (or ridge) is concerned, the S2 mode has about the same degree of westward tilt as the S1 mode. Our discussion on the comparison between the S1 and S2 modes is also applicable to the comparison of the A1 and A2 modes.

So far, we have considered the structure of unstable motions for zonal wavenumber $s = 4$. As seen from section 2, we anticipate that the structure of unstable motions depends on their longitudinal scale. Figures 16 and 17 are the same as Fig. 12, except they deal with zonal wavenumber $s = 8$, corresponding to almost the case of maximum instability. Comparing Figs. 12 and 16, we notice that the maximum amplitude of S1 for the case of $s = 8$ is located lower than the corresponding case of $s = 4$. In fact, the amplitude of S1 is pretty much constant throughout the lower troposphere with a slight reduction around the level $p/p_s = 0.65$. On the other hand, the vertical westward phase tilt of the S1 in the case of $s = 8$ is approximately one-half that of $s = 4$. Also, we notice that the northward and southward decrease of phase from about 40°N in the case of $s = 8$ is much more gradual than in the case of $s = 4$. The upper left panel of Fig. 18 shows the hori-

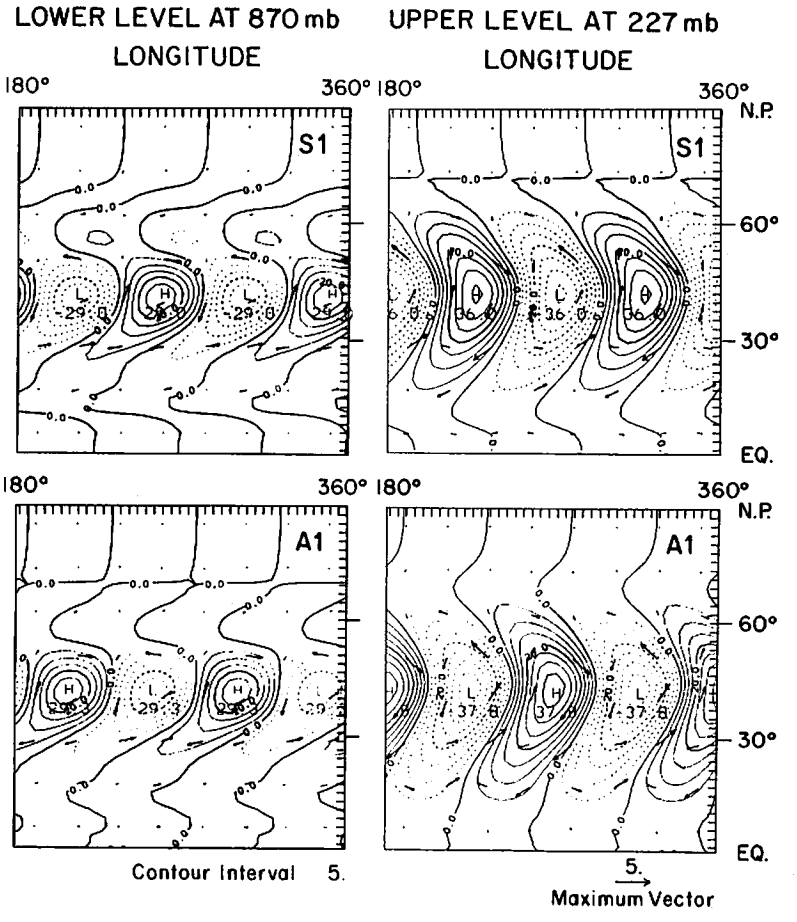

FIG. 13. Horizontal structures of S1 mode (upper panels) and A1 mode (lower panels) for zonal wavenumber 4 at the lower level $p/p_s = 0.870$ (left panels) and the upper level $p/p_s = 0.227$ (right panels). Only the Northern Hemisphere region from 180° to 360° in longitude is shown. The patterns are scaled so that the contour intervals are 5 m and the maximum velocity, indicated at the lower right-hand corner, is 5 m s^{-1}.

zontal structure of the S1 mode for zonal wavenumber $s = 8$ at the level $p/p_s = 0.87$. Comparison between the upper left panels of Figs. 18 and 13 shows clearly the dependence of the structure of unstable motions on their zonal wavenumber. Although the horizontal structure of the S1 mode for $s = 8$ at the upper level $p/p_s = 0.227$ is not shown here, it is not difficult to visualize that the upper level pattern is very similar to the lower level pattern except for the westward tilt of the system. Again, we see that the A1 mode is similar in its structure to the S1 mode.

The structure of the S2 mode for $s = 8$ looks quite different from the corresponding mode for $s = 4$, but a closer look shows some similarity. Figure 17 is the same as Fig. 14, except for $s = 8$. Actually, it is easier to comprehend Fig. 17a by first looking at the horizontal structure of the S2 mode for $s = 8$ at the lower level shown in the upper right panel of Fig. 18. We see a dipole structure with phase switch at 38°N and the amplitude maxima around 32° and 48°N. Now, let us look at Fig. 17a to visualize the vertical structure. The cell north of 38°N has a more intense and deeper structure with a smaller westward phase tilt than the cell south of 38°N. Therefore, in the upper troposphere, the horizontal structure of S2 is essentially dominated by the northern cell with a horizontal tilt in the north-northwest to south-southeast direction. When we look at Fig. 15 again for the structure of the S2 mode with $s = 4$, its lower tropospheric structure can be looked upon as a kind of dipole. Lastly, we can again see from Figs. 17 and 18 that the structures of the S2 and A2 modes are very similar.

e. Spectral energy distribution

One merit of the spectral method is its capability of representing the flow characteristics in terms of scales. While representation in terms of horizontal scales is fairly common, the scale representation in the vertical has not received much attention due primarily to lack of application of the analysis technique. With the use of three-dimensional normal mode expansions, we can

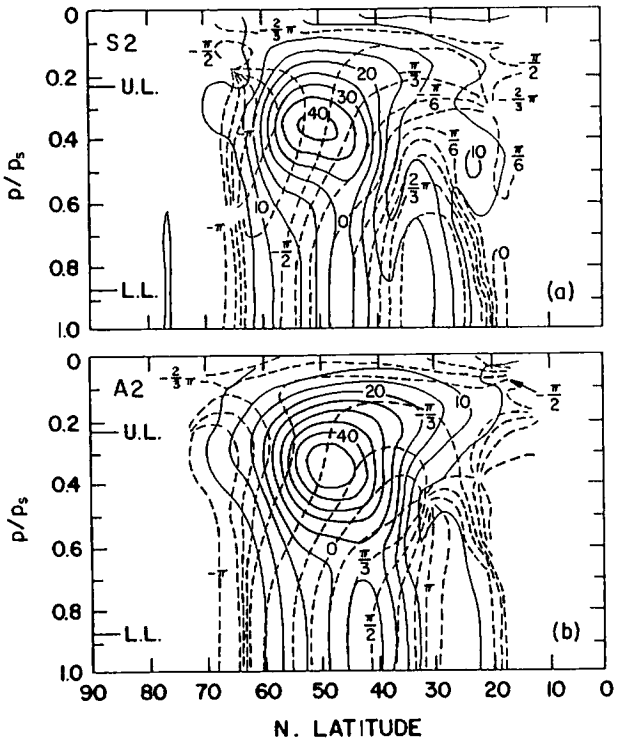

FIG. 14. As in Fig. 12, but (a) for the S2 mode, and (b) for the A2 mode.

examine the spectral distribution of energy not only in the horizontal scales, but also in the vertical scales (Kasahara and Puri 1981).

Figure 19 shows the spectral distribution of total energy (TE_r^s) defined by

$$(TE_r^s)_n = \frac{1}{2} gD_n C_r^s(n) C_r^{s*}(n) \qquad (3.14)$$

for the S1 and A1 modes in the case of $N = 6$ and $s = 8$. The ordinate shows the total energy and the abscissa denotes the meridional index. The index $r = -1$ represents the Kelvin mode, and $r = 0$ to 15 represent the rotational modes. The distributions of energy for six vertical modes are represented by different symbols shown in the inset. For example, the distribution for the external mode ($n = 1$) is shown by a solid line connecting the dots and the distribution for the third internal mode ($n = 4$) by a dashed line connecting the triangles. The case of $s = 8$ corresponds approximately to that of the maximum instability for the S1 and A1 modes. We see from Fig. 19 that the largest amount of energy resides in the large meridional scales ($r = 1 \sim 4$) of the external mode ($n = 1$) rotational components. The locations of energy peaks for the higher vertical modes tend to shift to higher meridional modes. This suggests that our meridional resolution is not enough for the vertical mode $n = 6$. Present findings demonstrate that the baroclinic instability in the westerlies can generate the external mode ($n = 1$) effectively. Note also that the Kelvin mode does not play a very significant role in the baroclinic instability examined here. General features of the energy spectral distributions shown in Fig. 19 resemble those of real data analyzed by Kasahara and Puri (1981) and Tanaka (1985).

Figure 20 shows the same quantities as Fig. 19, except (a) for the S2 mode and (b) for the A2 mode. The locations of energy peaks are generally shifted towards the medium meridional scales ($r = 5 \sim 10$) as reflected from the observations that the structure of the second most unstable modes contains more meridional complexity. From the fact that energy is not concentrated in the largest meridional and vertical scales, it is clear that more meridional and vertical modes are necessary to resolve accurately the structure of the higher (slower growing) unstable modes.

4. Discussion

We discuss here some remaining issues related to the use of vertical normal modes as the basis functions in the spectral discretization of prediction equations.

a. Lower boundary condition

One important topic which we have not discussed fully is the question of the lower boundary condition: whether the lower boundary condition, which is used to construct the vertical normal modes of the basic atmosphere at rest, can satisfy a more general lower boundary condition which incorporates the basic flow as done in this study. We will show below that it is indeed the case.

It is appropriate to choose the lower boundary condition $d\tilde{Z}'/d\tilde{t} = 0$ at $\sigma = 1$ in the original dimensional notation. This condition can be written explicitly as

$$\frac{\partial Z'}{\partial \tilde{t}} + \frac{\bar{u}}{a\cos\phi}\frac{\partial Z'}{\partial \lambda} + v'\frac{\partial \bar{Z}}{a\partial\phi} + \omega'\frac{dZ_0}{d\sigma} = 0, \qquad (4.1)$$

where we introduced a minor approximation that $\partial\bar{Z}/\partial\sigma$ is negligible compared with $dZ_0/d\sigma$ because of the observation that $\bar{T}(\sigma) \ll T_0(\sigma)$ (cf. Holton 1975).

The thermodynamic energy equation, before combining it with the continuity equation to derive the third equation in (2.10) of KS86, is given in the dimensional notation as

$$\frac{\partial}{\partial \tilde{t}}\left(\frac{-T'}{\Gamma_0}\right) + \omega' = \frac{1}{\Gamma_0}\left(\frac{\bar{u}}{a\cos\phi}\frac{\partial T'}{\partial\lambda} + \frac{v'}{a}\frac{\partial \bar{T}}{\partial\phi}\right), \qquad (4.2)$$

where

$$\Gamma_0 = \frac{\kappa T_0}{1+\sigma} - \frac{dT_0}{d\sigma}. \qquad (4.3)$$

In deriving (4.2), we assumed that $\partial\bar{Z}/\partial\sigma \ll dZ_0/d\sigma$ as in the case of (4.1).

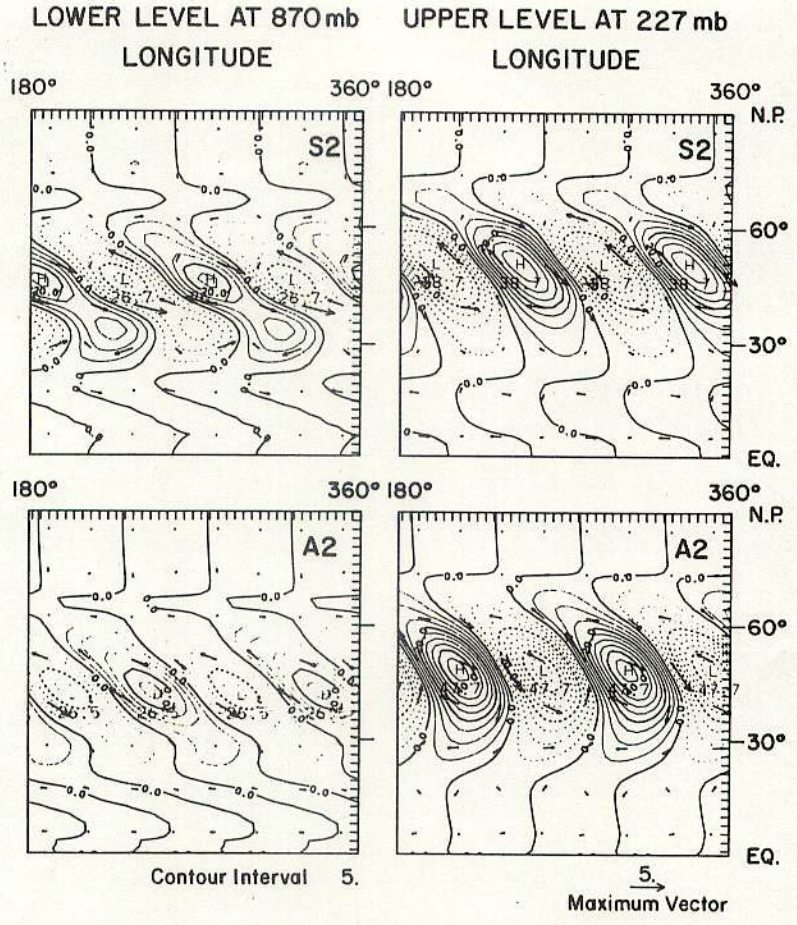

FIG. 15. As in Fig. 13, but the upper panels are for the S2 mode, and the lower panels are for the A2 mode.

The hydrostatic equilibrium is assumed between Z' and T' in the form

$$g\frac{\partial Z'}{\partial \sigma} = \frac{RT'}{1+\sigma}. \tag{4.4}$$

The same form of hydrostatic relation is assumed between $\bar{Z}$ and $\bar{T}$ and also Z_0 and T_0.

By substituting ω' from (4.1) into (4.2) and utilizing the hydrostatic relationships between (Z', T'), $(\bar{Z}, \bar{T})$ and (Z_0, T_0), we find that the lower boundary condition is expressed by

$$\left(\frac{\partial}{\partial t} + \frac{\bar{u}}{a\cos\phi}\right)\left(\frac{\partial Z'}{\partial \sigma} + rZ'\right) + \frac{v'}{a}\frac{\partial}{\partial \phi}\left(\frac{\partial \bar{Z}}{\partial \sigma} + r\bar{Z}\right) = 0, \tag{4.5}$$

where $r = \Gamma_0/T_0$ evaluated at $\sigma = 1$, which is identical to the symbol appearing in the lower boundary condition

$$\frac{dG_n}{d\sigma} + rG_n = 0 \quad \text{at} \quad \sigma = 1 \tag{4.6}$$

used to obtain the solutions of the vertical structure equation. Therefore, as long as the vertical structures of Z' and $\bar{Z}$ are expressed by the vertical structure functions G_n which satisfy the lower boundary condition (4.6), the lower boundary condition (4.5) is automatically satisfied.

b. *Accuracy of the solutions*

The accuracy of the numerical solutions with the normal mode expansions depends on two factors. One is the accuracy of the expansion functions as free solutions to the linearized system with respect to an atmosphere at rest. Since the construction of the normal mode functions is required to be performed only once as a precomputation, they should be calculated as accurately as possible. The other factor is the number of expansion functions for representation of the dependent variables. In the present case of a specified single zonal wavenumber, we only need to choose the number of expansion functions used in the meridional and vertical directions. In this regard, there is considerable freedom to choose from the ensemble of meridional modes involving the three different wave species. For example, we need to adopt only the rotational wave components of the meridional expansion functions if we wish to just represent quasi-geostrophic type mo-

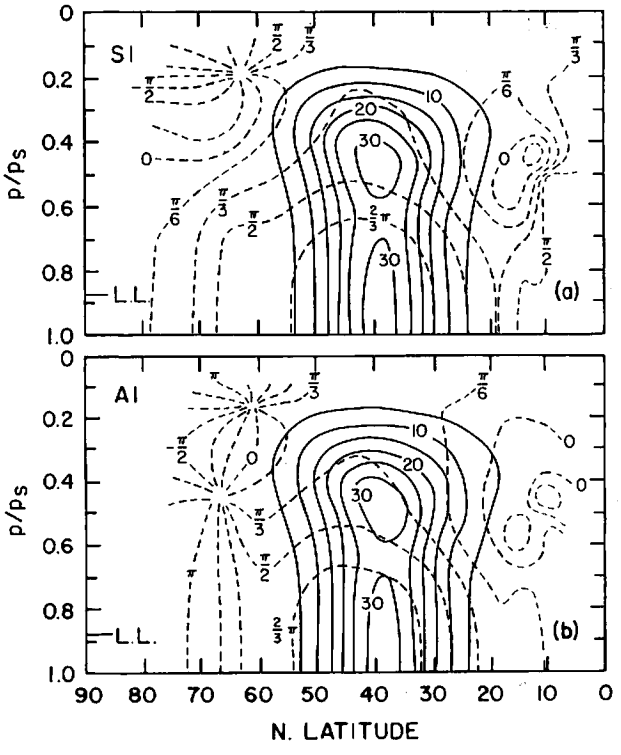

FIG. 16. As in Fig. 12, but for zonal wavenumber 8.

tions. The spectral distribution of total energy, such as discussed in section 3e, should be used to guide the selection of the appropriate resolution for both the meridional and vertical directions. There is no need to choose the same resolution of meridional expansion functions for all the vertical modes. A judicious choice of the meridional resolution as a function of the vertical mode should be able to economize numerical computations.

c. *Incorporation of orography*

This topic is not directly relevant to the problems of baroclinic instability discussed here, but it is important to comment on how the effects of mountains can be incorporated within the framework of vertical normal mode expansion. As shown by Kasahara and Puri (1981) and Staniforth et al. (1985), the vertical structure equation for the sigma coordinate system incorporating the effect of orography can be derived in the same way as discussed here with the aid of appropriate transformations of dependent variables. Therefore, essentially the same expansion procedure as described in this paper is applicable to the case of variable p_s with an addition of the prediction equation of p_s which can also be solved spectrally.

An interesting possibility along the same lines is that the use of the 3-D normal mode expansions may reduce a particular type of truncation error in sigma-system models. Because the horizontal coordinate surfaces are usually not parallel with either constant height or pressure surfaces in sigma-system models, a hydrostatic correction must be introduced to calculate the pressure gradient on the sigma surfaces. In a hybrid system of using the finite-difference method in the vertical with the spectral method in the horizontal, the type of truncation errors discussed by Sundqvist (1975) still remain in the evaluation of temperature which appears as a coefficient in the hydrostatic correction even though horizontal derivatives are calculated accurately by the spectral method. If this type of truncation error were reduced by adopting the spectral method in the vertical as well as in the horizontal, the 3-D spectral modeling will give a real advantage over the traditional hybrid formulation.

d. *Time integration*

One consideration which might have discouraged the subsequent exploration of the use of the spectral method in the vertical discretization of model variables was Francis' (1972) finding that a very small time step is needed when Laguerre polynomials are used as a basis. Again, this consideration is not relevant to the eigenvalue problems discussed in this paper, but a comment should be added in this regard in the event of using the explicit time differencing scheme for solution of the spectral equation (3.4). The form of the spectral equation (3.4) for each vertical mode is identical to the corresponding equation (5.2) in Kasahara (1977) for the global shallow water model and the computational stability of the centered time differencing scheme has been discussed in the same paper. Linear computational stability is related to the frequency

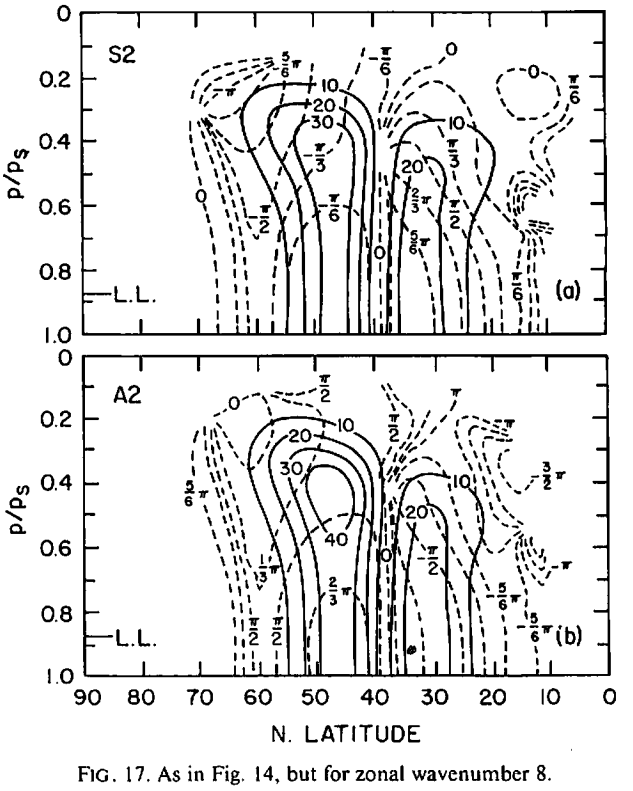

FIG. 17. As in Fig. 14, but for zonal wavenumber 8.

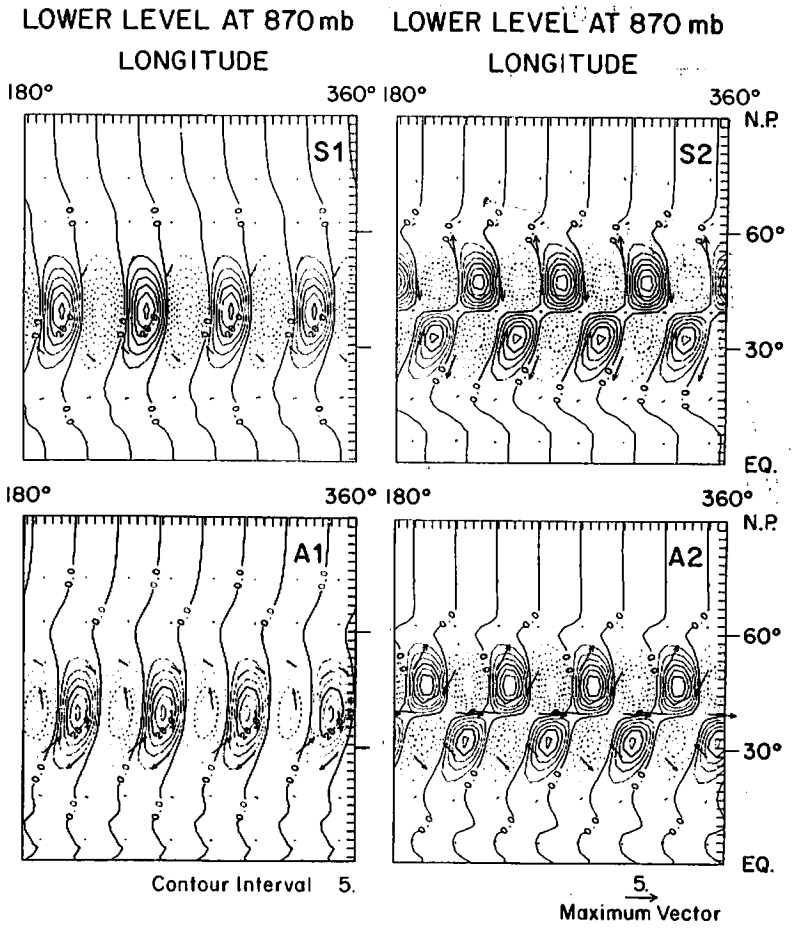

FIG. 18. Horizontal structures of S1 mode (upper left-hand panel), S2 mode (upper right-hand panel), A1 mode (lower left-hand panel) and A2 mode (lower right-hand panel) for zonal wavenumber 8. All are at the lower level $p/p_s = 0.870$.

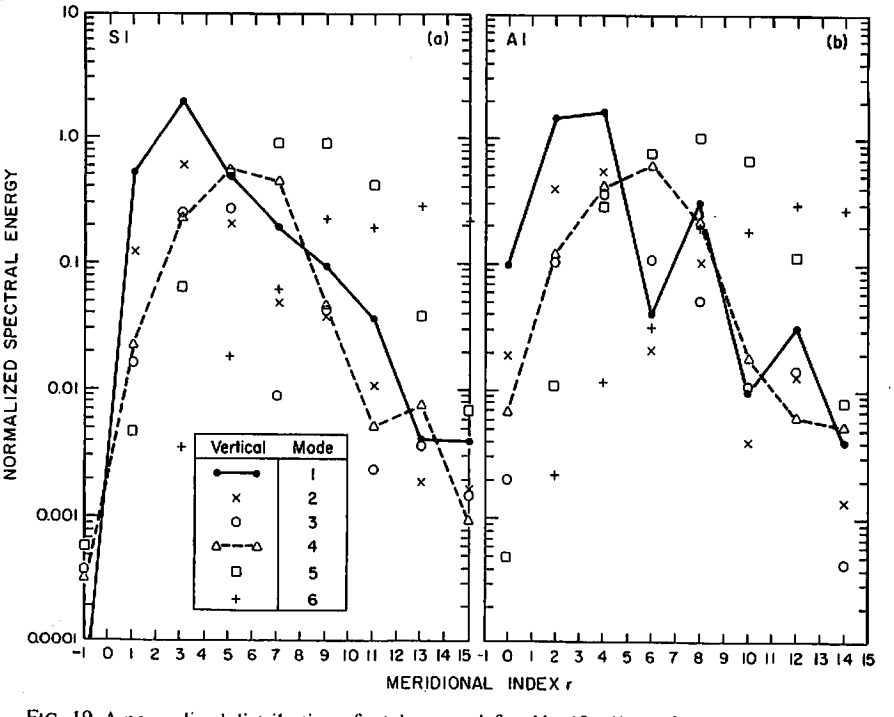

FIG. 19. A normalized distribution of total energy defined by (3.14) as a function of meridional index r shown on the abscissa and vertical mode n indicated in the inset: (a) for the S1 mode for zonal wavenumber 8, and (b) for the A1 mode for zonal wavenumber 8.

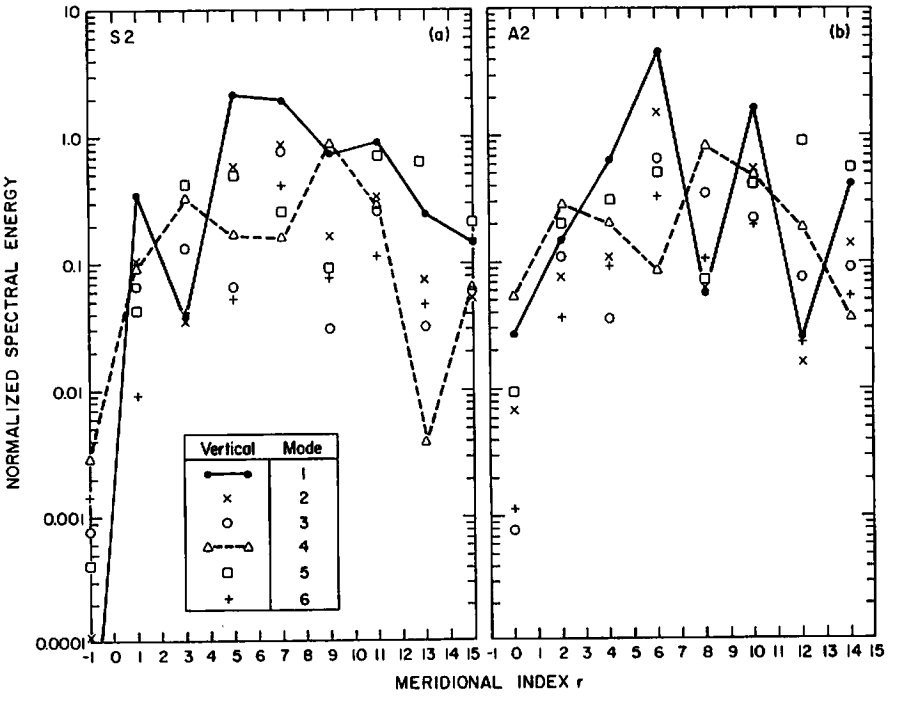

FIG. 20. As in Fig. 19, but (a) for the S2 mode and (b) for the A2 mode.

$\nu_r^s(n)$ corresponding to the expansion functions adopted. Because the linear part of the spectral equation (3.4) can be solved exactly using a transformation of the variables as discussed by Baer and Platzman (1961), the time step of integration is determined essentially by the frequency of slow meteorologically significant motions. Therefore, unlike the traditional global spectral models (e.g., Williamson 1983), there is no need to employ the semi-implicit time integration technique.

5. Conclusions

We investigated the use of normal mode expansion in discretizing model variables in the vertical for numerical solution of time dependent atmospheric equations. First, we reviewed briefly the past efforts of using the spectral method in the vertical discretization. No obvious reason was found as to why the use of spectral techniques has been rather unpopular compared with the finite-difference techniques in the vertical discretization, other than a shortage of references which demonstrate a potential usefulness. In this article, we are specifically concerned with the spectral method which uses the normal modes as the basis functions. The normal modes are obtained as the free solutions to dynamical systems.

As a simple example of vertical normal mode expansion, we examined the traditional baroclinic instability of Charney and Green types on a zonal flow with a constant vertical shear using a quasi-geostrophic potential vorticity equation. The normal modes were obtained analytically for an exponential temperature distribution in the vertical for the system without incorporating the basic flow. It was shown that the normal mode functions satisfy the upper and lower boundary conditions of the system incorporating the basic flow. The stability problem was then solved by applying the Galerkin method. The convergence of the numerical solutions was examined in detail by varying the spectral resolution. The results of the stability analysis are in general agreement with those obtained by previous investigators, indicating that the vertical normal mode expansion is a viable numerical approach to the problem.

The method of vertical normal mode expansion was extended to solve the problem of baroclinic instability on the sphere using the global primitive equation model linearized around a basic zonal flow with vertical and meridional shear. The 3-D normal modes, obtained as the free solutions to the linearized primitive equations without the effects of basic zonal flow, were used as the expansion functions. The evolution equations for the spectral coefficients of truncated series in the 3-D normal mode functions were derived by application of the Galerkin procedure. As a specific form of the basic zonal flow, the 30° jet adopted earlier by Simmons, Hoskins and Frederiksen was used. The stability of the 30° jet was investigated through the eigenvalue–eigenfunction approach. The growth rates and phase speeds of unstable motions were compared with those obtained by Simmons, Hoskins and Frederiksen using different techniques. The 3-D structures of symmetric and antisymmetric unstable motions were examined in detail.

A number of remaining issues were discussed in section 4. The presence of upper and lower boundary conditions in atmospheric modeling might have given the impression that the use of the spectral method may have disadvantages over the finite difference method. This appears to be a false impression, though it may be desirable to devote more research to exploring the characteristics of vertical normal mode functions under various boundary conditions (e.g., Platzman 1988). Comments were made concerning the treatment of the dynamical effect of orography in primitive equation modeling with the 3-D normal mode expansion as well as the method of time integration. These questions are not directly relevant to the specific problems investigated in this paper, but these discussions are necessary for a wider application of the 3-D normal mode expansion to atmospheric modeling. In conclusion, we find that not only is the vertical normal mode expansion a viable method for discretizing model variables in the vertical, but also the 3-D normal mode expansion provides a promising new avenue for numerical solution of the time-dependent primitive equations.

Acknowledgments. Partial support for this research has been provided at NCAR through the National Oceanic and Atmospheric Administration under P.O. NA85AAG02575 and at the University of Missouri-Columbia through the National Science Foundation under Grant ATM-8410487. The senior author wishes to thank G. W. Platzman for useful discussions regarding this research. The authors also thank G. Branstator, J. Frederiksen, J. Tribbia and two anonymous reviewers for their useful comments which are incorporated into this manuscript. Drafting of the figures was performed by the NCAR Graphics Department and the manuscript was typeset by R. Bailey and D. Raizman.

APPENDIX

The Form of Basic Zonal Flow and the Basic Temperature Distribution

The form of the 30° jet $\bar{u}(\phi, \sigma)$ as the basic zonal flow and the basic temperature distribution $T_0(\sigma)$ are specified following Hoskins and Simmons (1975) as

$$\bar{u}(\phi, \sigma) = \sin^2\pi\mu U_0(\sigma), \tag{A1}$$

where $\mu = \sin\phi$ and $\sigma = 2p/p_s - 1$. The functions $U_0(\sigma)$ and $T_0(\sigma)$ are constructed by fitting fifth-degree polynomials in σ to the values

$$U_0(\sigma) = (45, 35, 22, 12, 4)\ \text{m s}^{-1}$$

$$T_0(\sigma) = (220, 230, 250, 267, 280)\ \text{K}$$

at

$$\sigma = (-0.8, -0.4, 0, 0.4, 0.8)$$

respectively, with the additional conditions that $U_0'(1) = U_0'(0.8)$ and $T_0'(1) = T_0'(0.8)$ where the prime indicates differentiation with respect to σ. Figure A1 shows the function $U_0(\sigma)$ plotted against σ by solid line. The long and short dashed lines are its reconstruction using the series of vertical structure function $G_n(\sigma)$ with truncation $N = 6$ and 5, respectively. Notice that the profile of $U_0(\sigma)$ is approximated reasonably well by these series except for the lower atmosphere.

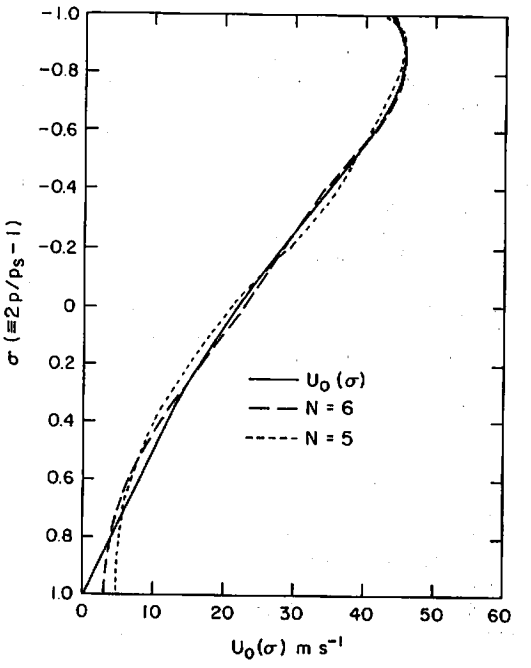

FIG. A1. Profile of $U_0(\sigma)$ as a function of σ. Short and long dashed lines are its reconstruction using the series of vertical structure function $G_n(\sigma)$ with truncation $N = 5$ and 6.

The static stability S is calculated from the definition

$$S = \frac{1}{T_*}\left(\frac{\kappa T_0}{1+\sigma} - \frac{dT_0}{d\sigma}\right). \tag{A2}$$

The dimensionless angular velocity for the basic zonal wind (A1) is given by

$$\bar{\alpha}(\phi, \sigma) = \bar{u}(\phi, \sigma)/(2a\Omega\cos\phi) = \bar{\alpha}_0(\phi)\sum_{l=1}^{N}\beta_l G_l(\sigma), \tag{A3}$$

where

$$\bar{\alpha}_0(\phi) = \sin^2\pi\mu/(1-\mu^2)^{1/2}, \tag{A4}$$

$$\beta_l = \int_{-1}^{1}\frac{U_0(\sigma)}{2a\Omega}G_l(\sigma)d\sigma. \tag{A5}$$

REFERENCES

Arakawa, A., and S. Moorthi, 1988: Baroclinic instability in vertically discrete systems. *J. Atmos. Sci.*, **45**, 1688–1707.

Baer, F., and G. W. Platzman, 1961: A procedure for numerical integration of the spectral vorticity equation. *J. Meteor.*, **18**, 393–401.

Bodin, S., 1974: The use of empirical orthogonal functions in quasi-geostrophic numerical prediction models. *Tellus*, **26**, 582–593.

Boyd, J., 1987: Orthogonal rational functions on a semi-infinite interval. *J. Comput. Phys.*, **70**, 63–88.

Charney, J. G., 1947: The dynamics of long waves in a baroclinic westerly current. *J. Meteor.*, **4**, 135–163.

Eckart, C., 1960: *Hydrodynamics of Oceans and Atmospheres.* Pergamon Press, 290 pp.

Finlayson, B. A., 1972: *The Method of Weighted Residuals and Variational Principles with Application in Fluid Mechanics, Heat and Mass Transfer.* Academic Press, 412 pp.

Francis, P. E., 1972: The possible use of Laguerre polynomials for representing the vertical structure of numerical models of the atmosphere. *Quart. J. Roy. Meteor. Soc.*, **98**, 662–667.

Frederiksen, J. S., 1978: Growth rates and phase speeds of baroclinic waves in multi-level models on a sphere. *J. Atmos. Sci.*, **35**, 1816–1826.

Fulton, S. R., and W. H. Schubert, 1980: Geostrophic adjustment in a stratified atmosphere. Atmos. Sci. Paper No. 326, Dept. of Atmospheric Sciences, Colorado State University, 97 pp.

Gall, R., and R. Blakeslee, 1977: Comments on "A note on the wavelength of maximum growth rate for baroclinic instability." *J. Atmos. Sci.*, **34**, 1479–1480.

Garcia, R. V., and R. Norscini, 1970: A contribution to the baroclinic instability problem. *Tellus*, **22**, 239–250.

Gavrilin, B. L., 1965: On the description of vertical structure of synoptical processes. *Izv. Acad. Sci. USSR, Atmos. Ocean. Phys.*, **1**, 8–17.

Geisler, J. E., and R. R. Garcia, 1977: Baroclinic instability at long wavelengths on a β-plane. *J. Atmos. Sci.*, **34**, 311–321.

Green, J. S. A., 1960: A problem in baroclinic stability. *Quart. J. Roy. Meteor. Soc.*, **86**, 237–251.

Grotjahn, R., 1987: Three-dimensional linear instability on a sphere: Resolution experiments with a model using vertical orthogonal basis functions. *J. Atmos. Sci.*, **44**, 3734–3752.

Hildebrand, F. B., 1958: *Methods of Applied Mathematics.* Prentice-Hall, 523 pp.

Hirota, I., 1968: On the dynamics of long and ultra-long waves in a baroclinic zonal current. *J. Meteorol. Soc. Jpn.* **46**, 234–249.

Holmström, I., 1963: On a method for parametric representation of the state of the atmosphere. *Tellus*, **15**, 127–149.

Holton, J. R., 1975: The Dynamic Meteorology of the Stratosphere and Mesosphere. *Meteor. Monogr.*, **15**(37), 216 pp.

Hoskins, B., 1973: Comments on: "The possible use of Laguerre polynomials for representing the vertical structure of numerical models of the atmosphere". *Quart. J. Roy. Meteor. Soc.*, **99**, 571–572.

——, and A. J. Simmons, 1975: A multi-layer spectral model and semi-implicit method. *Quart. J. Roy. Meteor. Soc.*, **101**, 637–655.

——, and M. J. Revell, 1981: The most unstable long wavelength baroclinic instability modes. *J. Atmos. Sci.*, **38**, 1498–1503.

Ioannou, P., and R. S. Lindzen, 1986: Baroclinic instability in the presence of barotropic jets. *J. Atmos. Sci.*, **43**, 2999–3014.

Jordan, C. L., 1958: Mean soundings for the West Indies area. *J. Meteor.*, **15**, 91–97.

Kasahara, A., 1977: Numerical integration of the global barotropic primitive equations with Hough harmonic expansions. *J. Atmos. Sci.*, **34**, 687–701.

——, 1978: Further studies on a spectral model of the global barotropic primitive equations with Hough harmonic expansions. *J. Atmos. Sci.*, **35**, 2043–2051.

——, 1982: Nonlinear normal mode initialization and the bounded derivative method. *Rev. Geophys. Space Phys.*, **20**, 385–397.

——, 1984: The linear response of a stratified global atmosphere to tropical thermal forcing. *J. Atmos. Sci.*, **41**, 2217–2237.

——, and K. Puri, 1981: Spectral representation of three-dimensional global data by expansion in normal mode functions. *Mon. Wea. Rev.*, **109**, 37–51.

——, and P. L. da Silva Dias, 1986: Response of planetary waves to stationary tropical heating in a global atmosphere with meridional and vertical shear. *J. Atmos. Sci.*, **43**, 1893–1911.

Kuo, H. L., 1979: Baroclinic instabilities of linear and jet profiles in the atmosphere. *J. Atmos. Sci.*, **36**, 2360–2378.

Lindzen, R. S., and K. K. Tung, 1978: Wave overreflection and shear instability. *J. Atmos. Sci.*, **35**, 1626–1632.

——, B. Farrell and K. K. Tung, 1980: The concept of wave overreflection and its application to baroclinic instability. *J. Atmos. Sci.*, **37**, 44–63.

Longuet-Higgins, M. S., 1968: The eigenfunctions of Laplace's tidal equations over a sphere. *Phil. Trans. Roy. Soc. London*, **A262**, 511–607.

Machenhauer, B., and R. Daley, 1972: A baroclinic primitive equation model with a spectral representation in three dimensions. Institute for Theoretical Meteorology, Copenhagen University, Rep. No. 4, 63 pp.

Obukhov, A. M., 1960: The statistically orthogonal expansion of empirical functions. *Izv. Akad. Nauk SSSR, Ser. Geogr. Geofiz.*, **3**, 288–291.

Pekeris, C. L., 1937: Atmospheric oscillations. *Proc. Roy. Soc. London*, **A158**, 650–671.

Platzman, G. W., 1960: The spectral form for the vorticity equation. *J. Meteor.*, **17**, 635–644.

——, 1988: The atmospheric lunar tide as a continuous spectrum. *Meteor. Atmos. Phys.*, **38**, 70–88.

Simmons, A. J., and B. J. Hoskins, 1976: Baroclinic instability on the sphere: Normal modes of the primitive and quasi-geostrophic equations. *J. Atmos. Sci.*, **33**, 1454–1477.

——, and ——, 1977: A note on the wavelength of maximum growth for baroclinic instability. *J. Atmos. Sci.*, **34**, 1477–1478.

Simons, T. J., 1968: A three-dimensional spectral prediction equation. Atmos. Sci. Paper No. 127, Dept. of Atmospheric Science, Colorado State University, 27 pp.

——, 1969: Baroclinic instability and atmospheric development. Atmos. Sci. Paper No. 150, Dept. of Atmospheric Sciences, Colorado State University, 36 pp.

Staley, D. O., 1986: Baroclinic and barotropic instability spectra as functions of N in N-level models. *J. Atmos. Sci.*, **43**, 1817–1832.

Staniforth, A. N., 1985: Finite-element modelling—some formulation considerations for atmospheric applications. *GARP Special Report*, No. 43, World Meteorological Organization, Geneva, Switzerland, 50–65.

——, M. Béland and J. Côté, 1985: An analysis of the vertical structure equation in sigma coordinates. *Atmos. Ocean*, **23**, 323–358.

Steppeler, J., 1987: Quadratic Galerkin finite element schemes for the vertical discretization of numerical forecast models. *Mon. Wea. Rev.*, **115**, 1575–1588.

Sundqvist, H., 1975: On truncation errors in sigma-system models. *Atmosphere*, **13**, 81–95.

Swarztrauber, P. N., and A. Kasahara, 1985: The vector harmonic analysis of Laplace's tidal equations. *SIAM J. Sci. Stat. Comput.*, **6**, 464–491.

Tanaka, H., 1985: Global energetics analysis by expansion into three-dimensional normal mode functions during the FGGE winter. *J. Meteor. Soc. Japan*, **63**, 180–200.

——, 1988: Normal mode energetics of the general circulation during the FGGE year. Ph.D. dissertation, University of Missouri, 79 pp.

Taylor, G. I., 1936: The oscillations of the atmosphere. *Proc. Roy. Soc. London*, **A156**, 318–326.

Valdes, P. J., and B. J. Hoskins, 1988: Baroclinic instability of the zonally averaged flow with boundary layer damping. *J. Atmos. Sci.*, **45**, 1584–1593.

Williamson, D. L., 1983: Description of NCAR Community Climate Model (CCMOB). NCAR Tech. Memo., NCAR/TN-210+STR. [Available from the National Center for Atmospheric Research, Boulder, CO 80307-3000.]